1 **Title:** Force generation by protein-DNA co-condensation

2

3 **Author list:** Thomas Quail[1,2,3,4], Stefan Golfier[1,2,3,4], Maria Elsner[1,2,3,4], Keisuke

4 Ishihara[1,2,3,4], Vasanthanarayan Murugesan[1,2,3,4], Roman Renger[1], Frank

5 Jülicher*[2,3,4], Jan Brugués*[1,2,3,4]

6

7 **Affiliations:**

8 [1]Max Planck Institute of Molecular Cell Biology and Genetics, 01307 Dresden, Germany
9 [2]Max Planck Institute for the Physics of Complex Systems, 01187 Dresden, Germany
10 [3]Center for Systems Biology Dresden, 01307 Dresden, Germany
11 [4]Cluster of Excellence Physics of Life, TU Dresden, 01307 Dresden, Germany
12 *correspondence: julicher@pks.mpg.de, brugues@mpi-cbg.de

13

14 **Abstract:** Interactions between liquids and surfaces generate forces[1,2] that are

15 crucial for many processes in biology, physics, and engineering, including the

16 motion of insects on the surface of water[3], modulation of the material properties

17 of spider silk[4], and self-assembly of microstructures[5]. Recent studies have shown

18 that cells assemble biomolecular condensates via phase separation[6]. In the

19 nucleus, these condensates are thought to drive transcription[7], heterochromatin

20 formation[8], nucleolus assembly[9], and DNA repair[10]. Here, we show that the

21 interaction between liquid-like condensates and DNA generates forces that might

22 play a role in bringing distant regulatory elements of DNA together, a key step in

23 transcriptional regulation. We combine quantitative microscopy, *in vitro*

24 reconstitution, optical tweezers, and theory to show that the transcription factor

25 FoxA1 mediates the condensation of a DNA-protein phase via a mesoscopic first-

26 order phase transition. After nucleation, co-condensation forces drive growth of

27 this phase by pulling non-condensed DNA. Altering the tension on the DNA strand

28 enlarges or dissolves the condensates, revealing their mechanosensitive nature.

29 These findings show that DNA condensation mediated by transcription factors

30 could bring distant regions of DNA in close proximity, suggesting that this physical

31 mechanism is a possible general regulatory principle for chromatin organization

32 that may be relevant *in vivo*.

33

34

Main text: Compartmentalization is key to organizing cellular biochemistry. Biomolecular condensate formation underlies the compartmentalization of many cellular functions[6]. Considerable progress has been made towards understanding the biophysical properties of condensates in bulk. However, how these condensates interact with other cellular components such as polymers, membranes, and chromatin remains unclear. Transcriptional hubs are an example of compartments in the nucleus. These hubs involve the coalescence of transcription factors, biochemical regulators of transcription, and DNA[11]. The physical nature of these transcription hubs is under debate, though recent studies have proposed that transcriptional hubs can be understood as examples of biomolecular condensates[12]. In theory, the interactions between transcriptional machinery condensates and the DNA polymer could deform DNA, potentially bridging distal regulatory elements, a critical step in gene regulation. However, we still lack a physical picture of how transcriptional regulators interact with each other and with the surface of the DNA polymer.

To investigate how transcription factors physically organize DNA, we attached linearized λ-phage DNA to a coverslip via biotin-streptavidin linkers (Fig. 1a). We used TIRF microscopy to image the interactions between DNA and Forkhead Box Protein A1 (FoxA1), a pioneer transcription factor that regulates tissue differentiation across a range of organisms[13] (Fig. 1b). Upon addition of 10 nM FoxA1-mCherry (FoxA1) to the flow chamber in the presence of DNA, FoxA1 formed protein condensates that decorated the strand (Fig. 1c). In the absence of DNA, FoxA1 did not nucleate condensates in solution at concentrations ranging from 10 to 500 nM (Extended Data Fig. 1a). The requirement for DNA in condensate formation at low concentrations suggests that DNA mediates the condensation of a thin layer of FoxA1 on DNA.

In our assay, DNA molecules displayed a broad distribution of end-to-end distances (L), determined by the DNA-coverslip attachment points (Fig. 1c, d). This end-to-end distance tunes the tension of the DNA[14]. For DNA strands with end-to-end distances greater than approximately 10 μm, FoxA1 generated protein condensates on DNA (Fig. 1c). However, FoxA1 condensation did not influence the

68   DNA molecule (Fig. 1c, leftmost pair of images). Strikingly, for DNA molecules with

69   end-to-end distances below 10 μm, FoxA1 pulled DNA into highly enriched

70   condensates of FoxA1 and DNA (Fig. 1c, Extended Data Fig. 1b-e) with a density of

71   roughly 750 molecules/μm³ (see Methods, Extended Data Fig. 2a-d). To quantify

72   FoxA1-mediated DNA condensation, we measured the cross-correlation of FoxA1-

73   DNA intensities as a function of end-to-end distance (see Methods, Fig. 1d,e,

74   Extended Data Fig. 3a). Consistent with the ability of FoxA1 to form FoxA1-DNA

75   condensates at low tensions, the cross-correlation decayed from one to zero with

76   increasing end-to-end distance (Fig. 1e). Thus, FoxA1 mediates the formation of a

77   DNA–protein-rich phase in a tension-dependent manner.

78

79   The observation that FoxA1 drives DNA condensation suggests that it can

80   overcome the DNA molecule's entropic tension set by the end-to-end distance[14].

81   Incorporating DNA into the condensates increases the tension on the strand,

82   thereby reducing the transverse DNA fluctuations of the non-condensed DNA. To

83   quantify this, we measured the DNA envelope width of the non-condensed DNA

84   fluctuations (see Methods, Extended Data Fig. 3b). In buffer, the DNA envelope

85   width decreased as a function of end-to-end distance, consistent with the

86   corresponding increase of DNA strand tension for increasing end-to-end

87   distances[14] (Fig. 1f). However, in the presence of FoxA1, the DNA envelope width

88   remained constant for all end-to-end distances as FoxA1 pulled DNA into one or

89   more condensates. The magnitude of the DNA envelope width was lower in the

90   presence of FoxA1 than in buffer conditions for all end-to-end distances (Fig. 1f).

91   Taken together, this suggests that FoxA1-DNA condensates generate forces that

92   can overcome the entropic tension of the non-condensed DNA and buffer its

93   tension.

94

95   The observation that FoxA1 can mediate DNA condensation suggests that it could

96   bridge distant DNA strands. To investigate this possibility, we examined DNA

97   molecules that were bound to the same streptavidin molecule at one end (Fig. 1g,

98   Extended Data Fig. 3c). In the absence of FoxA1, these DNA molecules form a v-

99   shaped morphology and fluctuate independently of one another. Upon addition of

100   FoxA1, however, we observed that the two strands zipped together, generating a

101   y-shaped morphology as the condensation of FoxA1 increased over time (Fig. 1g,

102   Extended Data Fig. 3c). Taken together, these data demonstrate that FoxA1 can

103   physically bridge DNA strands in both *cis* and *trans.*

104

105   Two mechanisms can be postulated to explain FoxA1-mediated DNA condensation

106   in our experiments: (i) direct cross-linking via the multiple DNA-binding activities

107   of FoxA1[15] or (ii) weak protein-protein interactions driven by disordered regions

108   of FoxA1. FoxA1 consists of a winged helix-turn-helix DNA-binding domain and

109   two N and C termini domains that are mostly disordered[15]. The DNA-binding

110   domain contains a sequence-specific binding region composed of three alpha

111   helices and a non-sequence-specific binding region composed of two wings. Two

112   point mutations known to affect sequence-specific DNA binding (NH-FoxA1[15]) had

113   virtually no influence on DNA condensation activity (Fig. 2a). Although the

114   presence of two point mutations known to affect non-sequence-specific DNA

115   binding (RR-FoxA1[15]) partially inhibited FoxA1 localization to the strand (Fig. 2b),

116   this mutant still condensed DNA. In this case, condensation occurred on a time

117   scale of minutes rather than seconds (as in WT-FoxA1), which can be explained by

118   the delay in condensing sufficient RR-FoxA1 to the strand. These data suggest that

119   non-sequence-specific binding drives the localization of FoxA1 to DNA but does

120   not mediate DNA condensation through cross-linking. Furthermore, the sequence-

121   specific binding domain of FoxA1 is dispensable for its localization to DNA *in vitro.*

122   To probe whether FoxA1 protein-protein interactions through disordered

123   domains mediate DNA condensation, we truncated both the N and C termini of

124   FoxA1. Although ΔN-FoxA1 retained DNA condensation activity (Fig. 2c),

125   truncating the disordered C terminus of FoxA1 largely inhibited DNA

126   condensation activity (Fig. 2d). Additionally, we found that, at high FoxA1

127   concentrations in bulk (50 μM), 3% PEG (30K) nucleated highly-enriched

128   spherical FoxA1 condensates (Extended Data Fig. 4a), further suggesting the

129   existence of weak FoxA1-FoxA1 interactions. Thus, non-sequence-specific binding

130   drives FoxA1 localization to DNA, and the disordered C terminus of FoxA1

131   promotes DNA condensation.

132

133 Our results support the hypothesis that FoxA1 condenses onto DNA to generate a

134 DNA–protein-rich condensate via weak protein-protein interactions that exerts a

135 pulling force on the non-condensed strand (see the section Thermodynamic

136 description of DNA-protein condensation in the Supplementary information). To

137 explore the thermodynamics of condensation, we developed a theoretical

138 description based on a semi-flexible polymer partially condensing into a liquid-

139 like condensate. Here, the semi-flexible polymer is DNA and the condensation is

140 mediated by the transcription factor. The free energy of this process contains

141 volume, $(v \frac{4}{3}\pi R^3)$, and surface contributions, $(\gamma 4\pi R^2)$, as well as a term

142 representing the free energy of the non-condensed DNA (Fig. 3a), where v is the

143 condensation free energy per volume, R is the condensate radius, and γ is the

144 surface tension of the condensate. We assume that DNA is fully collapsed inside

145 the condensate and thus its volume is proportional to the condensed DNA contour

146 length, $V = \alpha L_d$, where $1/\alpha$ describes the packing density given as DNA length

147 per condensate volume. The free energy of the polymer, $F_p(L, L_p) = \int_0^L f(L, L_p)\, dl$,

148 can be obtained from the force-extension curve of the polymer $f(L, L_p)$, where

149 L_p is the contour length of the non-condensed polymer. Using $L_p = L_c - L_d$ where

150 L_c is the contour length of λ-phage DNA (16.5 μm), the free energy is as follows,

151 $$F(L, L_d) = -v\alpha L_d + \gamma 4\pi \left(\frac{3\alpha}{4\pi}\right)^{\frac{2}{3}} L_d^{\frac{2}{3}}$$

152 $$+ \kappa \left(\frac{(L_c - L_d)^2}{4(L_c - L_d - L)} - \frac{L}{4} + \frac{L^2}{2(L_c - L_d)} - \frac{(L_c - L_d)}{4} \right)$$

153 where $\kappa = \frac{k_B T}{P}$, k_B is the Boltzmann constant, T is the temperature, and P is the

154 persistence length of DNA (see the section Thermodynamic description of DNA-

155 protein condensation in the Supplementary information). For fixed L, the

156 minimum of $F(L, L_d)$ determines the preferred size of the condensate. This free

157 energy predicts upon variation of L a stochastic first-order phase transition for the

158 formation of DNA–protein condensates (Fig. 3b). The distribution of condensate

159 sizes is then given by $P(L_d) \sim e^{-\beta F(L, L_d)}$ for fixed L (Fig. 3c). This accounts for a

160 sharp transition of DNA condensation controlled by the end-to-end distance and

161 thus the tension of the DNA molecule. The first-order nature of this behavior

162 implies regimes of hysteresis and bistability. Our theory also predicts that the

163 condensation forces exerted on the non-condensed DNA are kept roughly

164 constant.

165

166 To test this theory, we first measured DNA condensate volumes and found that

167 they increase linearly with the length of condensed DNA (L_d), with α=0.04 ± 0.01

168 μm² (Fig. 3d, Extended Data Fig. 4d, Methods). This confirms that DNA is in a

169 collapsed conformation inside the condensates. Next, we simultaneously fit the

170 predictions to the average amount of DNA contained in the condensates (L_d), and

171 the probability of nucleating a DNA condensate (P_{cond}) as a function of end-to-end

172 distance (see Methods). We calculated L_d (Fig. 3e, Extended Data Fig. 4e, Extended

173 Data Fig. 5) and P_{cond} (Fig. 3g, Extended Data Fig. 4f) using the Boltzmann

174 probability distributions (Fig. 3c) from the free energy. Our fits agree

175 quantitatively with the data and show that L_d decreases with L until a critical end-

176 to-end distance beyond which DNA condensates do not form. Below this critical

177 length, we observed that the force exerted by the condensate is buffered at 0.21

178 pN (0.18 – 0.30 pN CI), consistent with the theory (Fig. 3f). To complement our

179 force measurements, we performed optical tweezer measurements of FoxA1-

180 mediated DNA condensation. Incubating a single λ-phage DNA molecule at either

181 L = 6 or 8 μm in the presence of 150 nM FoxA1 generated forces on the order of

182 0.4-0.6 pN, consistent with the force measurements using fluorescence

183 microscopy (Methods, Extended Data Figs. 6,7). Finally, P_{cond} exhibits a sharp

184 transition at $L = 10.5$ μm (9.4 – 10.9 μm CI), in agreement with a stochastic first-

185 order phase transition (Fig. 3g). We also observed a sudden force jump during the

186 onset of condensate formation (as measured by the individual temporal force

187 trajectories in the optical tweezer experiments), consistent with a first order

188 phase transition (Extended Data Figs. 6c,7). Close to the transition point FoxA1-

189 mediated DNA condensation displayed bistability. This bistability was observed in

190 strands that contained multiple FoxA1 condensates, but where only some of them

191 condensed DNA (Extended Data Fig. 8a). Our fits allowed us to extract the physical

192 parameters associated with condensate formation, namely the condensation free

193 energy per volume υ = 2.6 pN/μm² (2.3 – 5.2 pN/μm² CI) and the surface tension

194 γ=0.04 pN/μm (0.04 – 0.28 pN/μm CI), see Methods section. These parameters are

195 consistent with previous measurements for *in vitro* and *in vivo* condensates[16,17].

196

197   Our theory and experiments show that two key parameters govern DNA–protein

198   co-condensation, namely the condensation free energy per volume (v) and the

199   surface tension (γ). We reasoned that different DNA-binding proteins may exhibit

200   a range of behaviors depending on these parameters. First, we investigated the

201   sequence-specific DNA-binding region mutant (NH-FoxA1), which also condensed

202   DNA but to a lesser extent (Fig. 2a). Quantitatively, we found that the surface

203   tension of condensates formed with this mutant was roughly unchanged

204   compared to WT-FoxA1, γ=0.065 pN/μm (0.05 – 0.07 pN/μm CI), but the free

205   energy per volume of condensation was reduced consistent with reduced DNA

206   binding, v=1.05 pN/μm^2 (0.9 – 1.1 pN/μm^2 CI), Extended Data Fig. 9, Fig. 4a. This

207   was also reflected in a decrease in the extent of DNA packing with α = 0.09 ± 0.02

208   μm^2 (Extended Data Fig. 9a). We also observed that NH-FoxA1-mediated

209   condensates generated a force of 0.17 pN (0.16 – 0.19 pN, CI), lower than that for

210   WT-FoxA1. In addition, NH-FoxA1 displayed bistable DNA–protein condensation

211   activity in the neighborhood of the transition point (Extended Data Fig. 8b). Next,

212   we examined the interactions of a different transcription factor Tata-Box-binding

213   protein (TBP) with DNA. We found that TBP also formed small condensates on

214   DNA, but did not condense DNA even at the lowest imposed DNA tensions (Fig.

215   4b). Instead, TBP performed a diffusive motion along the DNA strand (Extended

216   Data Fig. 10c), suggesting that DNA-protein condensation is not

217   thermodynamically favored. Another transcription factor, Gal4-VP16, formed

218   condensates on DNA and condensed DNA in a tension-dependent manner

219   consistent with FoxA1 (Extended Data Fig. 10e). Lastly, we analyzed somatic

220   linker histone H1, a protein that is structurally similar to FoxA1. However, in

221   contrast to FoxA1, one of the known functions of H1 is to compact chromatin[18], so

222   we expected H1 to strongly condense DNA. Consistent with this, we found that H1

223   displayed a stronger DNA condensation activity compared to FoxA1, condensing

224   DNA for all measured end-to-end distances (Fig. 4c). Interestingly, the *Xenopus*

225   embryonic linker histone B4 condensed DNA in a tension-dependent manner but

226   not to the same extent as H1 (Extended Data Fig. 10f). Thus, we propose that the

227   competition between condensation free energy per volume of the DNA–protein

228   phase and surface tension regulate a spectrum of DNA condensation activities,

229   which may be tuned by the structure of transcription factors.

230

231   Here, we show that FoxA1 can condense DNA under tension to form a DNA–

232   protein-rich phase that nucleates through a force-dependent first-order transition

233   for forces below a critical value. This critical force, which is on the order of 0.2-0.6

234   pN for FoxA1, is set by co-condensation forces that the DNA–protein phase exerts

235   on the non-condensed DNA. These forces are similar in magnitude to those

236   recently measured for DNA loop extrusion on the order of 0.2-1 pN[19,20] and those

237   estimated in intact nuclei from nuclear condensate fusion[21]. Thus, we speculate

238   that these weak forces we find *in vitro* may be of relevance to the mechanics of

239   chromatin organization, though future studies are necessary to show this. Taken

240   together, our work suggests that co-condensation forces may act as an additional

241   mechanism to remodel chromatin in addition to molecular motors that extrude

242   loops and complexes that remove or displace nucleosomes (Fig. 4d).

243

244   Transcription-factor-mediated DNA–protein condensation represents a possible

245   mechanism by which transcription factors coordinate enhancer-promoter

246   contacts in transcriptional hubs[12]. In this context, DNA–protein condensates could

247   act as scaffolds, pulling co-factors into the droplet (Fig. 4d). Our theoretical

248   description reveals that these DNA–protein condensates are formed via a first-

249   order phase transition, suggesting that they can be assembled and disassembled

250   rapidly by changing mechanical conditions. Near the transition point, assembly

251   and disassembly of these *in vitro* DNA–protein condensates becomes highly

252   stochastic, reminiscent of the rapid dynamics associated with the initiation and

253   cessation of transcriptional bursts observed in vivo[22].

254

255   We have demonstrated that protein-DNA co-condensation is associated with a

256   difference in chemical potential between the condensed and non-condensed DNA.

257   This difference in chemical potential is transduced by the condensate to perform

258   mechanical work on the non-condensed DNA strand. Capillary forces represent

259   another example of forces that involve liquid-surface interactions[1,2,23]. With both

260   co-condensation and capillary forces, attractive interactions give rise to the

261   transduction of free energy into work. Such forces may also be relevant beyond

262   chromatin in other biological contexts, including membranes and the

263   cytoskeleton.

264

265   DNA–protein co-condensation not only provides mechanisms to facilitate

266   enhancer–promoter contacts, but could also play a more general role in DNA

267   compaction and maintenance of bulk chromatin rigidity in processes such as

268   mitotic chromatid compaction[24], and the formation of chromatin

269   compartments[8,25,26]. Owing to the tension-dependent nature of DNA–protein co-

270   condensation, our work suggests that these forces could play a key and, as yet,

271   underappreciated role in genome organization and transcriptional initiation. It is

272   appealing to imagine that transcriptional outputs not only respond to

273   concentrations of transcription factors in the nucleus, but also to mechanical cues

274   from chromatin.

275

276   **References:**

277   1.   De Gennes, P.-G., Brochard-Wyart, F. & Quere, D. *Capillarity and Wetting*
278   *Phenomena*. Springer (2013).
279   2.   Bico, J., Reyssat, É. & Roman, B. Elastocapillarity: When Surface Tension
280   Deforms Elastic Solids. *Ann. Rev. Fluid Rev.* **50,** 629-659 (2017).
281   3.   Hu, D.L. & Bush, J. W. M. The hydrodynamics of water-walking arthropods.
282   *J. Fluid Mech.* **664,** 5-33 (2010).
283   4.   Elettro, H., Neukirch, S., Vollrath, F. & Antkowiak, A. In-drop capillary
284   spooling of spider capture thread inspires hybrid fibers with mixed solid–
285   liquid mechanical properties. *Proc. Natl. Acad. Sci. USA* **113,** 6143–6147
286   (2016).
287   5.   Mastrangeli, M. *et al.* Self-assembly from milli- to nanoscales: methods and
288   applications. *J. Micromech. Microeng.* **19,** 083001–38 (2009).
289   6.   Hyman, A. A., Weber, C. A. & Jülicher, F. Liquid-Liquid Phase Separation in
290   Biology. *Annu. Rev. Cell Dev. Biol.* **30,** 39–58 (2014).
291   7.   Sabari, B. R. *et al.* Coactivator condensation at super-enhancers links phase
292   separation and gene control. *Science* **361,** eaar3958–13 (2018).
293   8.   Larson, A. G. *et al.* Liquid droplet formation by HP1α suggests a role for
294   phase separation in heterochromatin. *Nature* **547,** 236–240 (2017).
295   9.   Feric, M. *et al.* Coexisting Liquid Phases Underlie Nucleolar
296   Subcompartments. *Cell* **165,** 1686–1697 (2016).
297   10.   Patel, A. *et al.* A Liquid-to-Solid Phase Transition of the ALS Protein FUS
298   Accelerated by Disease Mutation. *Cell* **162,** 1066–1077 (2015).
299   11.   Furlong, E. E. M. & Levine, M. Developmental enhancers and chromosome
300   topology. *Science* **361,** 1341–1345 (2018).

301 12. Cramer, P. Organization and regulation of gene transcription. *Nature* **573**,
302   45-54, (2019).
303 13. Zaret, K. S. & Mango, S. E. Pioneer transcription factors, chromatin
304   dynamics, and cell fate control. *Curr. Opin. Genet. Dev.* **37,** 76–81 (2016).
305 14. Bustamante, C., Marko, J. F., Siggia, E. D. & Smith, S. Entropic elasticity of
306   lambda-phage DNA. *Science* **265,** 1599–1600 (1994).
307 15. Sekiya, T., Muthurajan, U. M., Luger, K., Tulin, A. V. & Zaret, K. S.
308   Nucleosome-binding affinity as a primary determinant of the nuclear
309   mobility of the pioneer transcription factor FoxA. *Genes Dev.* **23,** 804–809
310   (2009).
311 16. Jawerth, L. M. *et al.* Salt-Dependent Rheology and Surface Tension of
312   Protein Condensates Using Optical Traps. *Phys. Rev. Lett.* **121,** 258101
313   (2018).
314 17. Brangwynne, C. P. *et al.* Germline P granules are liquid droplets that
315   localize by controlled dissolution/condensation. *Science* **324,** 1729–1732
316   (2009).
317 18. Botao, X. *et al.* Histone H1 compacts DNA under force and during
318   chromatin assembly. *Mol. Biol. Cell.* **23,** 4864-4871 (2012).
319 19. Golfier, S., Quail, T., Kimura, H. & Brugués, J. Cohesin and condensin
320   extrude DNA loops in a cell-cycle dependent manner. *Elife* **9,** (2020).
321 20. Banigan, E. J. & Mirny, L. A. Loop extrusion: theory meets single-molecule
322   experiments. *Curr. Opin. Cell Biol.* **64,** 124–138 (2020).
323 21. Shin, Y. *et al.* Liquid Nuclear Condensates Mechanically Sense and
324   Restructure the Genome. *Cell* **175,** 1481–1491 (2018).
325 22. Fukaya, T., Lim, B. & Levine, M. Enhancer Control of Transcriptional
326   Bursting. *Cell* **166,** 358–368 (2016).
327 23. Jang, J., Schatz, G. C., & Ratner, M. A. Capillary force in atomic force
328   microscopy. *J. Chem. Phys.* **120,** 1157-1160 (2004).
329 24. Yoshimura, S. H. & Hirano, T. HEAT repeats – versatile arrays of
330   amphiphilic helices working in crowded environments? *J. Cell. Sci.*
331   jcs.185710–8 (2016).
332 25. Strom, A. R. *et al.* HP1α is a chromatin crosslinker that controls nuclear
333   and mitotic chromosome mechanics. *bioRxiv* **29,** 717–742 (2020).
334 26. Williams, J. F. *et al.* Phase separation enables heterochromatin domains to
335   do mechanical work. *bioRxiv* **78,** 236–245 (2020).
336 27. McCall, P. M. *et al.* Quantitative phase microscopy enables precise and
337   efficient determination of biomolecular condensate composition. *bioRxiv*
338   **16,** 2885–19 (2020).
339 28. Shakya, A., Park, S., Rana, N. & King, J. T. Liquid-Liquid Phase Separation of
340   Histone Proteins in Cells: Role in Chromatin Organization. *Biophys. J.* **118,**
341   753–764 (2020).
342 29. Turner, A. L. *et al.* Highly disordered histone H1−DNA model complexes
343   and their condensates. 1–6 (2018). doi:10.1073/pnas.1805943115
344
345

359

360 **Author contributions:** T.Q. and J.B. conceived the project. T.Q. and S.G. performed
361 imaging experiments. S.G. established the single-strand DNA assay. T.Q. purified
362 proteins, made constructs, and performed data analysis. T.Q., J.B., and F.J.
363 performed theoretical calculations. M.E. made the TBP and Gal4-VP16 constructs
364 and purified the proteins. V.M. purified B4. T.Q. and R.R. performed optical
365 tweezer measurements. S.G. and R.R. performed data analysis and contributed to
366 methods writing. K.I. made the initial FoxA1 construct and provided key
367 biochemical support. J.B. and F.J. supervised the work. T.Q., J.B., and F.J. wrote the
368 manuscript and all authors contributed ideas and reviewed the manuscript.

369

370 **Competing interest statement:** The authors declare no competing financial
371 interests.

372
373
374
375
376
377
378
379
380
381
382
383
384
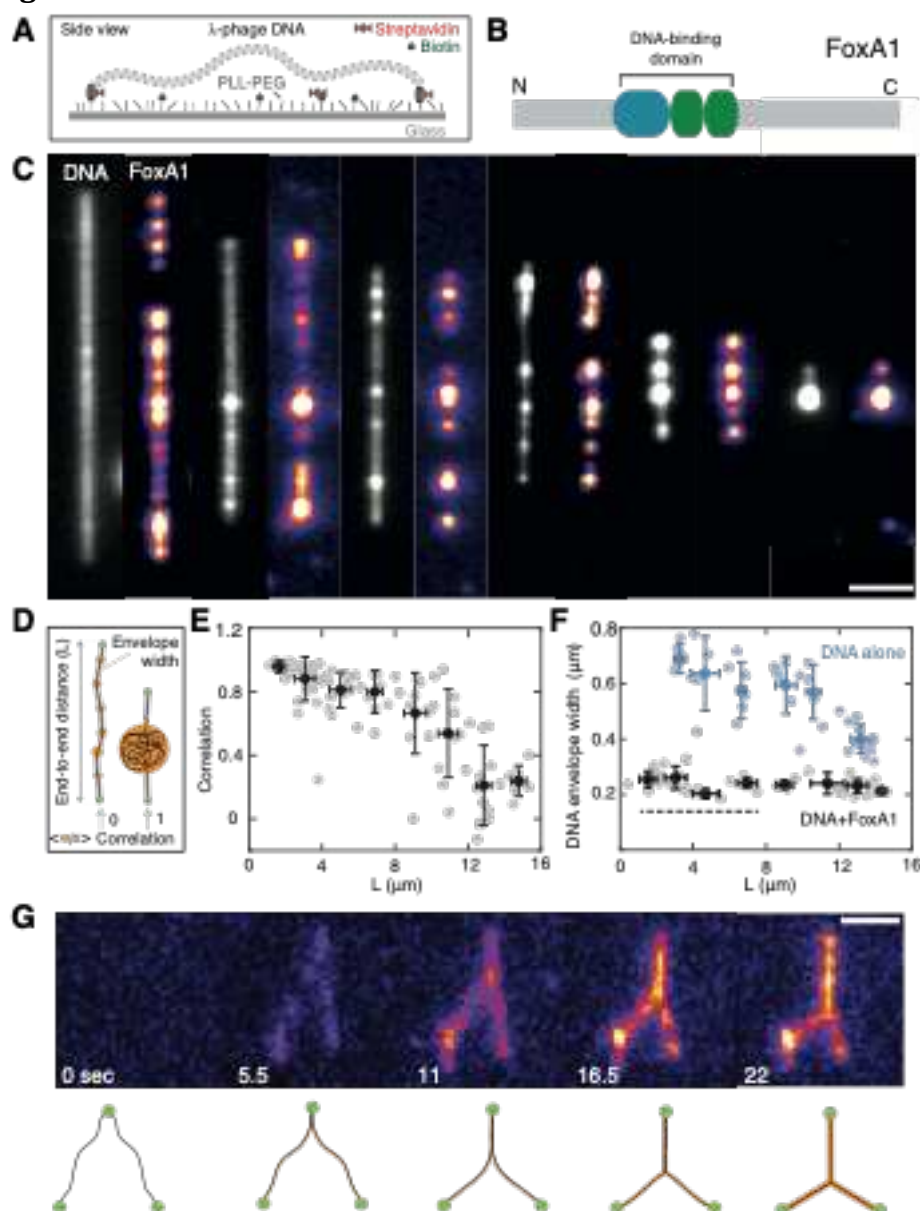385
386

387 **Figure 1**

388
389 **Figure 1: FoxA1 forms DNA-FoxA1 condensates in a tension-dependent**
390 **manner.** (A) Schematic of single λ-phage DNA molecule assay. (B) Structure of
391 FoxA1, consisting of a structured DNA-binding domain flanked by mostly
392 disordered N and C termini. The DNA-binding domain has a sequence-specific
393 binding region (blue) and two non-sequence-specific binding regions (green). (C)
394 The extent of FoxA1-mediated DNA condensation depends on the end-to-end
395 distance of the strand. Representative time-averaged projections of FoxA1 and
396 DNA. Note that the total amount of DNA is the same in each example. The DNA was
397 imaged using 10 nM Sytox Green. Scale bar=2 μm. (D) Schematic displaying three
398 main quantities used to characterize DNA-FoxA1 condensation: the end-to-end
399 distance L; Cross-correlation of DNA and FoxA1 intensities; and DNA envelope
400 width, a measure of transverse DNA fluctuations. (E) Cross-correlation of FoxA1
401 and DNA signals shows that FoxA1 condenses DNA below a critical end-to-end
402 distance. The gray dots represent individual strands, n=107. The data is binned
403 every 2-μm (black, mean ± SD for both correlations and strand lengths). (F) DNA

404 envelope width measurements (see Methods) reveal that FoxA1-DNA
405 condensation buffers DNA tension (blue and black dots correspond to control and
406 DNA+FoxA1 conditions, n=45 and n=50 respectively). The data is binned every 2-
407 μm (mean ± SD for both the envelope widths and strand lengths). The dashed
408 black line represents the theoretical diffraction limit. (G) Representative images
409 of FoxA1 zipping two independent DNA strands over time. Scale bar=2 μm.
410
411
412
413
414
415
416
417
418
419
420
421
422
423
424
425
426
427
428
429
430
431
432
433
434
435
436
437
438
439
440
441
442
443
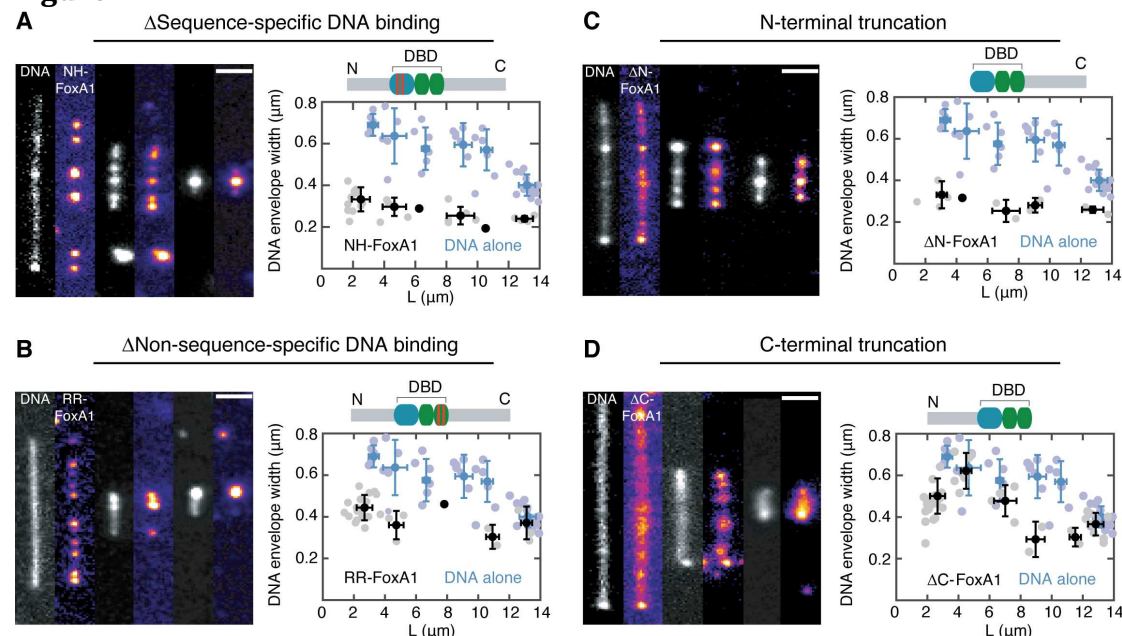444
445
446
447
448
449
450
451
452

Figure 2

Figure 2: Mutant analysis reveals that the C terminus of FoxA1 drives DNA condensation. Representative images and DNA envelope width measurements for FoxA1 mutants. The data is binned every 2-µm and the mean ± SD (for both the envelope width and the strand length) are shown in black for each mutant and in blue for control (n=45). Scale bars=2 μm. (A) Sequence-specific DNA binding mutant NH-FoxA1 condenses DNA (n=30). (B) Non-sequence-specific DNA-binding mutant RR-FoxA1 condenses DNA (n=28). (C) N-terminal truncation of FoxA1 ΔN-FoxA1 condenses DNA (n=13). (D) C-terminal truncation of FoxA1 ΔC-FoxA1 inhibits DNA condensation (n=44). In all conditions, the protein concentration was 10 nM.
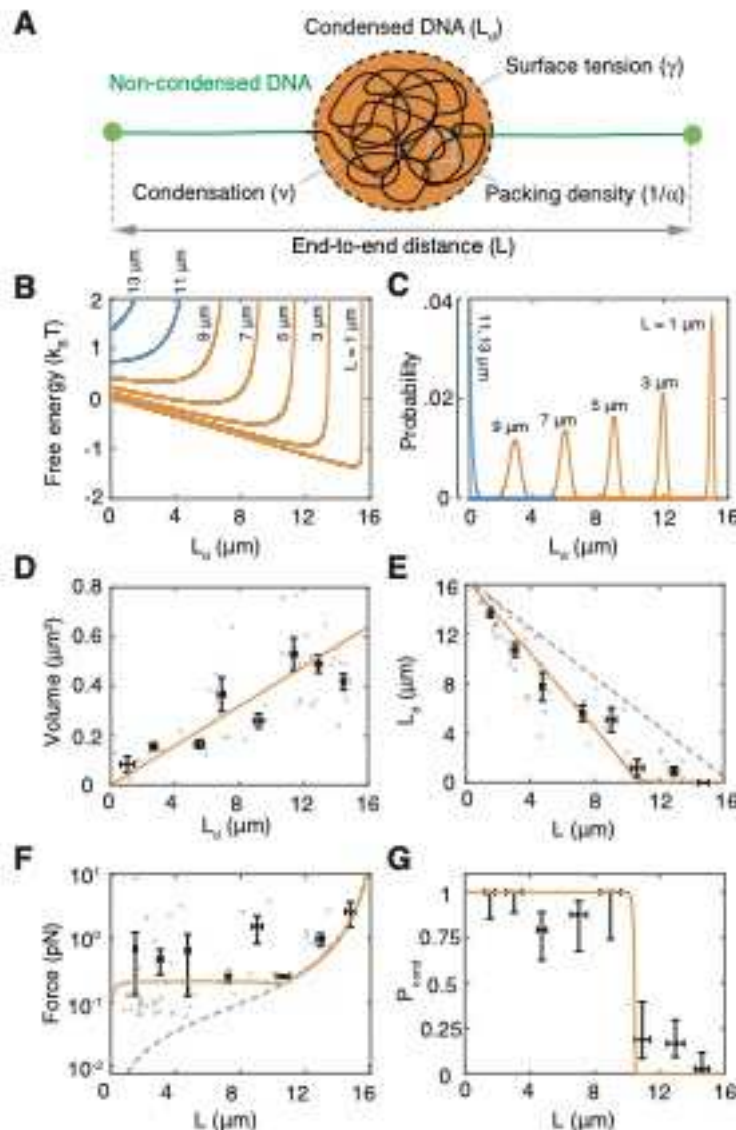
Figure 3

Figure 3: Thermodynamic description of a liquid phase condensing onto a semi-flexible polymer explains FoxA1-mediated DNA condensation. (A) Schematic representing DNA-FoxA1 condensation (orange). DNA can be in a condensed state (black) or a non-condensed state (green). DNA condensation depends on the condensate surface tension (γ), condensation free energy per volume (v), and DNA packing efficiency (α). (B) Free energy profiles as a function of condensed DNA (L_d) for different L reveal a first-order phase transition for DNA–protein condensation (orange and blue correspond to favorable and unfavorable condensation, respectively). (C) Boltzmann distributions corresponding to the free energy profiles in (B). (D) Condensate volume linearly increases with L_d. The orange curve represents a linear fit to individual strands (n=47). For (D), (E), and (F), individual strands are represented as gray dots and binned mean±SEM is in black. (E) Amount of condensed DNA as a function of L (n=63) reveals sharp transition. Orange curve represents optimal theoretical fit. The gray dashed-line corresponds to the limit of maximum condensation where L_d is equal to the contour length of DNA (16.5 μm) minus L. (F) Condensation forces that DNA-protein condensates exert on non-condensed DNA are buffered (n=62). Orange curve is the theoretical prediction. The gray dashed line

15

505 represents the force when $L_d=0$. (G) Probability to nucleate a DNA-FoxA1
506 condensate (P_{cond}) reveals a sharp transition at a critical end-to-end distance. P_{cond}
507 is computed from binned local correlation data (n=181 condensates). The end-to-
508 end distance error bars are the SD and the P_{cond} error bars are the 95% confidence
509 intervals from a Beta distribution.
510
511
512
513
514
515
516
517
518
519
520
521
522
523
524
525
526
527
528
529
530
531
532
533
534
535
536
537
538
539
540
541
542
543
544
545
546
547
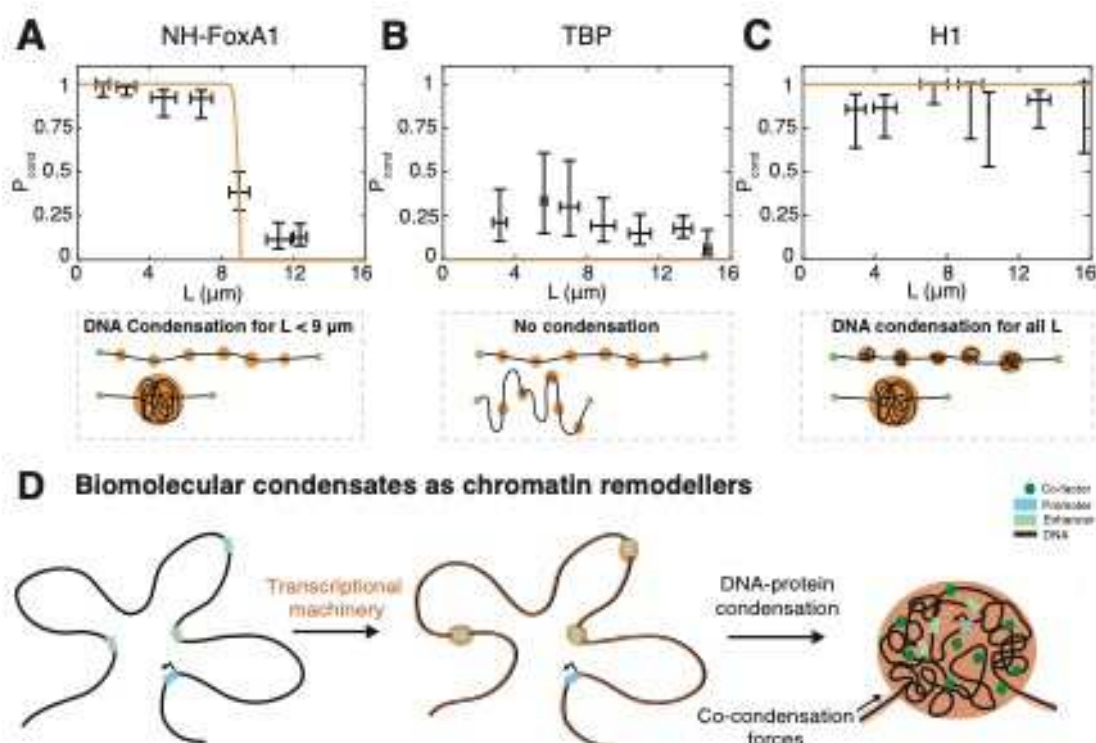548
549
550
551
552
553 **Figure 4**

Figure 4: Universality of protein-DNA co-condensation. Probability to form a protein-DNA co-condensate for NH-FoxA1 (A), Tata-box-binding protein (B), and Somatic linker histone H1 (C). P_{cond} is computed from local correlation data with n=361 condensates for NH-FoxA1 (A), n=247 condensates for Tata-box-binding protein (B), and n=101 for H1 (C). Scale bar=2 μm. The error bars for the end-to-end distance are SD and the P_{cond} error bars are the 95% confidence intervals from a Beta distribution. We found that NH-FoxA1 condensed DNA less strongly than WT-FoxA1, TBP could not condense DNA for any end-to-end distance, and H1 condensed DNA for all measured end-to-end distances. (D) Biomolecular condensates generate condensation forces that could serve to recruit transcriptional regulators, and potentially remodel chromatin at physiologically relevant force scales in order to properly regulate transcription. See Figure 2 in the Supplementary Information for representative protein-DNA images of NH-FoxA1, TBP, and H1.

Methods

584

585 Cloning and protein purification

586 FoxA1-mCherry was introduced into a bacterial expression vector with an N-
587 terminal His$_6$ tag using Gateway cloning. Unlabeled FoxA1 was cloned and purified
588 the same way. This vector was transformed into T7 express cells (enhanced BL21
589 derivative, NEB C2566I), grown to OD~0.4-0.8, whereupon we added 1 mM IPTG
590 and expressed His$_6$-FoxA1-mCherry for 3-4 hours at 37°C. We thawed frozen
591 pellets in binding buffer (1xBB) that contained 20 mM Tris-HCl (pH=7.9), 500 mM
592 NaCl, 20 mM Imidazole, 1 mM MgCl$_2$, supplemented with protease inhibitors and
593 Benzonase. The redissolved pellets were lysed and clarified via centrifugation.
594 Discarding the supernatant, we resuspended the pellets in 1xBB + 6 M Urea, spun,
595 collected the supernatant and poured it over an IMAC column, eluting the protein
596 with 1xBB+6 M Urea+250 mM Imidazole. We dialyzed overnight into storage
597 buffer (1xSB), 20 mM HEPES (pH=6.5), 100 mM KCl, 1 mM MgCl$_2$, 3 mM DTT, and
598 5 M Urea. Multiple dialysis rounds reduced the concentration of urea. Finally, the
599 protein was dialyzed into 1xSB+2 M Urea, spun-concentrated to 4-5 mg/ml (~50
600 µM), and then snap-frozen nitrogen and stored at -80°C. NH-FoxA1-mCherry and
601 RR-FoxA1-mCherry were obtained following[15] using the Q5 Site-Directed
602 Mutagenesis Kit. The truncation constructs were generated using restriction
603 digestion-ligation approaches coupled with PCR. We used Alexa-488-labeled
604 somatic linker histone H1 purified from calf thymus (H-13188, ThermoFisher). To
605 purify mCherry-B4, the gene (Genscript) was cloned into a bacterial expression
606 vector with N-terminal His$_6$ and mCherry tags, transformed into T7 express cells,
607 grown to OD~0.7 and supplemented with 0.8 mM IPTG and expressed at 37°C for
608 four hours. Resuspending the pellets in lysis buffer, 1xPBS with 500 mM NaCl, 1
609 mM DTT plus protease inhibitors and Benzonase, we then lysed the cells, collected
610 the supernatant, ran the supernatant over an IMAC column, and eluted the protein
611 with lysis buffer+250 mM Imidazole. The protein was dialyzed into 1xPBS+500
612 mM NaCl overnight, spun-concentrated, snap-frozen, and stored at -80 °C. We
613 purified labeled versions of Tata-box binding protein and Gal4-VP16 using similar
614 purification strategies. Both vectors—His$_6$-MBP-eGFP-zTBP and His$_6$-Gal4-GFP-
615 VP16—were transformed into T7 express cells, grown to OD~0.6, whereupon we
616 added 0.2 mM IPTG and expressed overnight at 18 °C. We lysed the cells into

617   buffer containing 50 mM Tris-HCl (pH=8.0), 1 M NaCl, 10% glycerol, 1 mM DTT, 1

618   mM $MgCl_2$ supplemented with protease inhibitors. For subsequent steps, 10 μM

619    $ZnSO_4$ was added to buffers for the Gal4-VP16 purification. After lysis, we added

620   NP40 to 0.1% and clarified via centrifugation. We performed a polyethylenimine

621   precipitation to precipitate DNA and then an ammonium sulfate precipitation to

622   recover the protein, resuspending the precipitated proteins in buffer containing

623   50 mM Tris-HCl (pH=8.0), 1 M NaCl, 10% glycerol, 1 mM DTT, 0.1% NP40, and 20

624   mM imidazole and clarified the soluble fraction via centrifugation. We poured the

625   lysate over an IMAC column and eluted the protein using 2xPBS, 250 mM

626   imidazole, 10% glycerol, and 1 mM DTT. We pooled protein fractions and dialyzed

627   TBP overnight into 20 mM HEPES pH=7.7, 150 mM KCl, 10% glycerol, and 1 mM

628   DTT and Gal4-VP16 into 20 mM Hepes (pH=7.7), 100 mM KCl, 50 mM Sucrose, 0.1

629   mM $CaCl_2$, 1 mM $MgCl_2$, 1 mM DTT, and 10 μM $ZnSO_4$. We then spun-concentrated

630   the proteins, snap-froze using liquid nitrogen, and stored at -80°C.

631

632   <u>DNA functionalization, cover slip PEGylation, and DNA micro-channel preparation</u>

633   To biotinylate DNA purified from λ-phage (λ-phage DNA), we followed the

634   protocol given in[19]. Each end of the biotinylated λ-phage DNA had two biotin

635   molecules. To PEGylate the cover slips and prepare the DNA microchannels we

636   followed the protocol given in[19].

637

638   <u>DNA and protein imaging</u>

639   We fluorescently stained immobilized DNA strands with 10 nM Sytox Green in

640   Cirillo buffer (20 mM HEPES, pH=7.8, 50 mM KCl, 2 or 3 mM DTT, 5% glycerol, 100

641   μg/ml BSA). For experiments with H1 and TBP, we imaged DNA using 25 nM Sytox

642   Orange. We used protein concentrations of 10 nM. We used a Nikon Eclipse

643   microscope with a Nikon 100x/NA 1.49 oil SR Apo TIRF and an Andor iXon3

644   EMCCD camera using a frame-rate of 100 – 300ms. A highly inclined and laminated

645   optical sheet (HILO) was established using a Nikon Ti-TIRF-E unit mounted onto

646   the microscope stand.

647

648   <u>Optical tweezer measurements</u>

649   We performed optical tweezer experiments using a C-Trap G2 system (Lumicks)

650   in a microfluidics flowcell (Lumicks), providing separate laminar flow channels.

651   For each experiment, we trapped two streptavidin-coated polystyrene beads

652   (Spherotec SVP-40-5). Once trapped, we moved these beads to a channel

653   containing biotinylated λ-phage DNA (Lumicks) at a concentration of 0.5 μg/ml,

654   whereupon we used an automated "tether-finder" routine to capture a single

655   molecule between the two beads. Once a single λ-phage DNA molecule was

656   attached to the two beads, we moved the trapped beads to a buffer-only channel

657   (containing Cirillo buffer: 20 mM HEPES, pH=7.8, 50 mM KCl, 3 mM DTT, 5%

658   glycerol, 100 μg/ml BSA). In the buffer-only channel, we fixed the molecule's end-

659   to-end distance at either L=6 or 8 μm. We then moved the tethered DNA to a

660   channel containing 150 nM FoxA1 in Cirillo buffer or another buffer-only channel

661   (as a control) and tracked the force and imaged the FoxA1-mCherry fluorescence

662   for 100 seconds.

663

664   <u>Bulk phase separation assays</u>

665   We performed bulk phase separation assays with FoxA1-mCherry, NH-FoxA1-

666   mCherry, and somatic linker histone H1. The storage buffer for FoxA1 and NH-

667   FoxA1 was 20 mM HEPES (pH=6.5), 100 mM KCl, 1 mM $MgCl_2$, 3 mM DTT, and 2

668   M Urea. The storage buffer for H1 was 1xPBS. For FoxA1, we combined 6 μl of

669   FoxA1 (at 50 μM) and 1 μl of 20% 30K poly-ethylene glycol (PEG). For NH-FoxA1,

670   we combined 9 μl and 1 μl of 20% 30K PEG. For H1, we combined 9 μl H1 and 1 μl

671   100 μM 32-base pair ssDNA. We prepared flow channels with double-sided tape

672   on the cover slide and attached a PEGylated cover slip to the tape. We imaged the

673   condensates using spinning disk microscopy and a 60x objective.

674

675   <u>FoxA1 molecule number estimation</u>

676   To estimate the number of FoxA1-mCherry molecules per condensate, we

677   quantified the intensity of single FoxA1-mCherry molecules bound non-

678   specifically to the slide. Around each segmented spot of DNA-independent FoxA1

679   intensity, we cropped an area of 10x10 pixels, performed a background

680   subtraction and summed the remaining intensity in the cropped area. To

681   determine the contribution of the background, the same method was applied to

682   10x10 pixel areas void of FoxA1 signal intensity. The resulting distribution of
683   these integrated signal intensities reveals consecutive peaks that are evenly
684   spaced by an average intensity of about 400 a.u., allowing us to calculate the
685   number of molecules. This approach should interpreted as a   lower bound
686   estimate of the number of FoxA1-mCherry molecules per condensate, as it
687   neglects effects such as fluorescent quenching[27].

688

689   Hydrodynamic stretching of DNA

690   DNA molecules bound at only one end to the slide were hydrodynamically
691   stretched using a constant flow rate of 100 µl/min of 0.5 nM FoxA1-mCherry in
692   Cirillo buffer with 10 nM Sytox Orange. The flow rate was sustained for tens of
693   seconds using a programmable syringe pump (Pro Sense B.V., NE-501).

694

695   Strand length calculation

696   To calculate the end-to-end distance, we generated time-averaged projections of
697   FoxA1 and DNA and integrated these projections along the strand's orthogonal
698   axis. To find the profile's "left" edge, we computed the gradient of the signal and
699   determined the position where the gradient went through a threshold (defined as
700   0.2). We then took all the points from the start of the signal to this position,
701   performed a background subtraction, and fit an exponential to these points. To
702   ensure that we included the entire DNA signal, we defined the fitted threshold for
703   both the left and the right edges as three-quarters of the value of the fitted
704   exponential value at the point when the gradient had gone through the intensity
705   threshold. Using this fitted threshold, we computed the position values for the left
706   and the right sides, and computed the end-to-end distance as the difference
707   between these two positions.

708

709   Global cross-correlation analysis

710   We generated time-averaged projections from movies of both FoxA1 and DNA, and
711   then summed the intensities in the orthogonal axis to the strand, generating line
712   profiles. We then calculated the strand length and cropped both the FoxA1 and
713   DNA line profiles from the edges of the strand. We then subtracted the mean value
714   from these cropped line profiles, normalized the amplitudes of the signals by their

21

715   Euclidean distances, and computed the zero-lag cross-correlation coefficient of

716   the normalized signals, which we defined as "Correlation": $R(\tau = 0) = \sum_{n=1}^{N} \overline{x_n}\overline{y_n}$,

717   where τ is the number of lags, N is the number of points in the normalized FoxA1

718   and DNA signals, $\overline{x_n}$ is the nth entry of the normalized FoxA1 signal, and $\overline{y_n}$ is the

719   nth entry of the normalized FoxA1 signal. In general, Correlation values range

720   from -1 to 1, but in our experimental data the values range from roughly 0 to 1,

721   where 1 represents the formation of DNA-FoxA1 condensates and 0 represents

722   the formation of only FoxA1 condensates (no DNA condensation).

723

724   DNA envelope width calculation

725   To compute the DNA envelope width, we first generated time-averaged

726   projections from movies of FoxA1 and DNA. We then selected segments of the

727   strand that did not contain FoxA1—regions of non-condensed DNA. Using these

728   segments, we extracted a line profile of the DNA signal orthogonal to the strand

729   that gave the maximum width. We then subtracted off the background of the DNA

730   profile, normalized the signal's amplitude using the Euclidean distance, and fit a

731   Gaussian. We defined the DNA envelope width as $\sqrt{2}\sigma$, which represents the

732   square root of two times the standard deviation of the fitted Gaussian. The

733   theoretical diffraction limit is calculated using the Rayleigh criterion, a measure of

734   the minimal resolvable distance between two point sources in close proximity for

735   a given set of imaging conditions: $d = \frac{0.61\,\lambda}{NA}$, where λ represents the imaging

736   wavelength and NA is the numerical aperture. For our imaging setup, d = 0.2 μm,

737   which is approximately 2σ of the fluorescent source from the DNA. As the DNA

738   envelope width is defined as $\sqrt{2}\sigma$, our "diffraction limit" as given by the dashed

739   line in Fig. 1f is given as 0.14 μm.

740

741   Condensate volume analysis

742   To calculate condensate volumes, we generated time-averaged DNA-FoxA1

743   projections and then localized the peaks of the DNA condensates. Using the peak

744   locations, we extracted background-subtracted one-dimensional profiles of the

745   DNA condensates in the orthogonal axis to the strand—these profiles went

746   through the peak location. We fit Gaussians to these profiles without normalizing

22

747 the amplitude. To define the radii of the condensates, we computed the gradient

748 of the fitted Gaussians and defined the condensate "edges" as when the absolute

749 value of the gradient of the Gaussian function gradient went through a threshold

750 value (defined as one, and determined by comparing with fluorescence).

751 Assuming condensates are spherical, we computed the condensate volume as $V =$

752 $\frac{4}{3}\pi R^3$, where R is the condensate's radius. To compute a condensate volume for

753 strands with multiple condensates, we simply added up the volumes for each

754 condensate.

755

756 <u>Condensed DNA amount analysis</u>

757 To compute the amount of condensed DNA, L_d, we generated time-averaged

758 projections of DNA and FoxA1 signals, integrating the DNA signal in the orthogonal

759 direction to the strand. We then defined condensed vs non-condensed DNA with

760 Threshold$_{\text{drop}}$: the median value of the profile plus a tolerance. Intensity values

761 below Threshold$_{\text{drop}}$ were defined as pixels of non-condensed DNA, and intensity

762 values above Threshold$_{\text{drop}}$ were defined as pixels of condensed DNA. This

763 assumption was also consistent with the measured FoxA1 signal, where FoxA1

764 signals clearly localized to regions of condensed DNA, as defined by the

765 Threshold$_{\text{drop.}}$ The tolerance value was used to suppress artefactual fluctuations

766 of the non-condensed DNA signal in the neighborhood of the median. To optimize

767 the tolerance value, we assume that L_d as a function of L is linear for lower values

768 of L (<5 μm) with a y-intercept equal to the contour length of the DNA molecule

769 (16.5 μm), as this is consistent with our theoretical description. We plotted the y-

770 intercepts of the linear fits as a function of tolerance and found that tolerance=500

771 gives a y-intercept equal to 16.5 and generates DNA-FoxA1 condensates up to 10

772 μm consistent with our data and analysis (Extended Data Fig. 6). To calculate the

773 DNA length contained within the droplet, we integrated the intensities from pixels

774 above Threshold$_{\text{drop}}$, divided this value by the sum of the total intensity of the

775 profile, and then multiplied this ratio by the contour length of λ-phage DNA, 16.5

776 μm. The non-condensed DNA length was calculated as simply the contour length

777 minus L_d. We used the same tolerance = 500 for the NH-FoxA1 mutant analysis.

778

779 <u>Force analysis</u>

23

780   To calculate the force that the condensate exerts on the non-condensed DNA, we

781   used the worm-like chain model, which relates λ-phage DNA's extension and force.

782   Upon addition of FoxA1, the amount of non-condensed DNA reduces, and the

783   extension changes as follows, $E = \frac{L}{L_c - L_d}$, where L_d is the amount of condensed

784   DNA, L is the end-to-end distance, and L_c is the total contour length of the

785   molecule. We then directly compute the force using the worm-like-chain model,

786    $F = \kappa \left(\frac{1}{4} (1 - E)^{-2} - \frac{1}{4} + E \right)$

787

788   <u>Condensate nucleation probability analysis</u>

789   To calculate the probability of the formation of a DNA-protein condensate as a

790   function of end-to-end distance, we localized the peaks of the FoxA1 condensates

791   from time-averaged projections of FoxA1 and DNA. We then extracted 0.9 μm x

792   0.5 μm windows centered around the localized FoxA1 peaks of both the FoxA1 and

793   DNA signals—with the window's long axis going with the strand and the short axis

794   as orthogonal to the strand. We then computed the zero-lag normalized cross-

795   correlation coefficient as follows:

796    $$C_{loc} = \frac{\sum \sum (f(x,y) - \mu_f)(g(x,y) - \mu_g)}{\sqrt{\sum f(x,y)^2 - \mu_f^2} \sqrt{\sum g(x,y)^2 - \mu_g^2}}$$

797   where $f(x,y)$ is the DNA, $g(x,y)$ is FoxA1, μ_f is the mean of the DNA image, and

798   μ_g is the mean of the FoxA1 image. This generates values from -1 to 1. For FoxA1-

799   mediated DNA condensation, the values for particular condensates are close to 1.

800   When FoxA1 fails to condense DNA, owing to the morphology of the underlying

801   DNA strand and the small number of pixels, we obtain values that range from -1 to

802   roughly 0.5. To obtain a value for P_{cond} as a function of end-to-end distance, we

803   selected a threshold of 0.75—C_{loc} values above the threshold are considered as

804   "condensed" and values below would be considered "non-condensed". We binned

805   the C_{loc} data in 2-μm increments as a function of end-to-end distance, and

806   calculated P_{cond} by taking the number of "condensed" condensates and dividing it

807   by the total number of condensates within the bin. The confidence intervals for

808   P_{cond} in each respective bin are computed by computing the 95% confidence

809   interval of a beta-distribution, which represents the probability distribution for a

810 Bernoulli process that takes into account the total number of successes with

811 respect to the total number of attempts.

812

813 <u>Parameter fitting of the thermodynamic description and confidence intervals</u>

814 To fit α, we used a linear fit of the condensate volumes for individual strands as a

815 function of L_d. The confidence intervals are the 95 per cent CI generated from

816 directly fitting the points. To fit the surface tension γ and condensation free energy

817 per volume v, we minimized the error of the average $\overline{L_d}(L)$ and $P_{cond}(L)$ with

818 respect to the data to optimize the parameter values. We used the normalized

819 Boltzmann distribution $P(L_d) = \frac{e^{-\beta F(L,L_d)}}{\int_0^{L_c-L} e^{-\beta F(l)} dl}$ to calculate $\overline{L_d} = \int_0^{L_c-L} l P(l) dl$. To

820 compute $P_{cond}(L)$, we localized the position of the local maximum in the free

821 energy, L_d^{max} for a given L and then computed the probability to "not" nucleate a

822 droplet from the Boltzmann distribution $\int_0^{L_d^{max}} P(l) dl$, which gives $P_{cond} = 1 -$

823 $\int_0^{L_d^{max}} P(l) dl$. To minimize the error, we binned the data in 2-μm-width bins. For

824 each "binned" mean for both condensed DNA and condensation probability, we

825 computed the squared residual of the mean value with respect to the theoretical

826 expression. For residuals calculated from $\overline{L_d}(L)$, we normalized each residual by

827 the squared standard error of the mean, and then summed the normalized

828 residuals to obtain the error. For residuals calculated from $P_{nuc}(L)$, we normalized

829 each residual by the variance of the beta distribution, $P_{nuc} \sigma^2_{cond} = \frac{(1+k)(1-k+N)}{(2N^2(3+N))}$ and
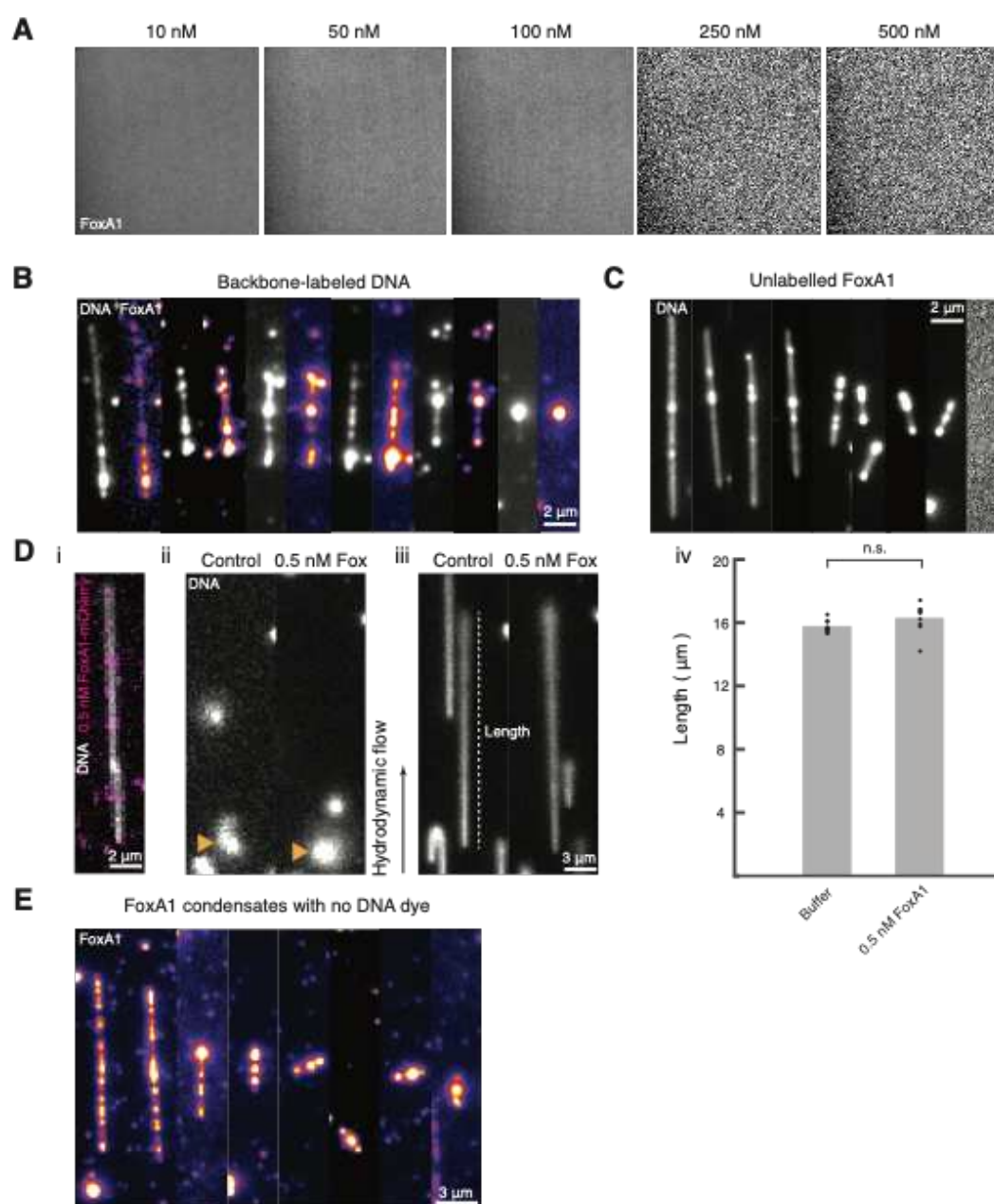
830 then summed the normalized residuals to obtain the error. For the global error,

831 we simply added the error from both deviations in $\overline{L_d}(L)$ and $P_{cond}(L)$. We then

832 iterated through a range of values for (γ, v) and computed the total error

833 associated with each set of parameter values, exponentiated the negative values

834 of the total error matrix, and computed the largest combined value to select the

835 parameter values. To calculate the parameters' confidence intervals, we obtained

836 one-dimensional profiles of the integrated exponentiated total error for v as a

837 function of γ and γ as a function of v. The peaks of these profiles represented the

838 values that we selected for our best-fit parameters. We assumed that these profiles

839 represented probability distributions for parameter selection, and then calculated

840 the left and right bounds where the area under the curve between these bounds

841   represented 95 per cent of the area. These left and right bounds represent the

842   lower and upper values of our confidence intervals. To compute the 95 per cent

843   confidence intervals for the force for each respective end-to-end distance value,

844   we scanned through (γ, υ) parameter space and computed the value of L_d for each

845   set of parameters. We then plotted these values against the probability that these

846   parameter values were the "true" values—simply the probability from the

847   exponentiated error matrix. Integrating the points under the Probability vs. L_d

848   curve and dividing this by the total area under this curve, we generated a

849   probability distribution function from which we could compute the 95%

850   confidence intervals for L_d. Because the force was constant, to compute the

851   confidence intervals for the force, we calculated the force using the worm-like

852   chain model using corresponding L_d values for an end-to-end distance that

853   retained FoxA1-mediated DNA condensation. To compute the confidence intervals

854   for L_{crit}, we scanned through (γ, υ) parameter space and computed L_{crit} for each

855   set of parameters. We then plotted L_{crit} values with the corresponding values

856   from the probability that these parameter values were true (again, the

857   exponentiated error matrix). Integrating the points under the Probability vs L_{crit}

858   curve and dividing this by the total area under this curve, we generated a

859   probability distribution function from which we could compute the 95%

860   confidence intervals for L_{crit}.

861

862   **Data availability statement:** Source data files are made available for this paper.

863   Data generated and analysed supporting the findings of this manuscript will be

864   made available upon reasonable request.

865

866   **Code availability statement:** Code generated supporting the findings of this

867   manuscript will be made available upon reasonable request.

868

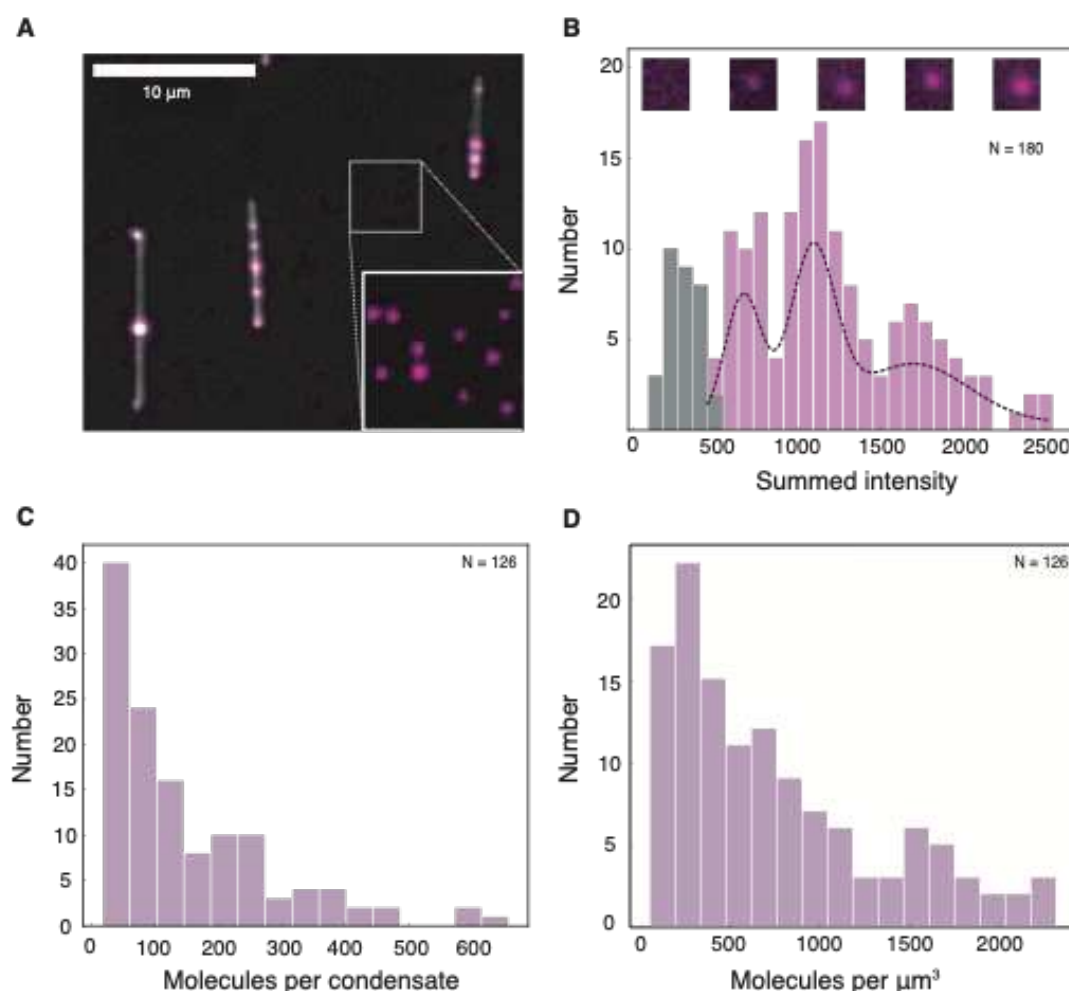869

870

871

872

873

874

875

876

877 **Extended Data Figure 1**

878

879 **Extended Data Figure 1: Experimental controls for FoxA1-mediated DNA**
880 **condensation.** (A) Representative fluorescent images of FoxA1-mCherry in buffer
881 (20 mM HEPES, pH=7.8, 50 mM KCl, 2 mM DTT, 5% glycerol, 100 µg/ml BSA) at
882 different concentrations, 10-500 nM, in the absence of DNA reveals that FoxA1
883 does not form condensates in bulk at these concentrations. Using spinning disk
884 microscopy and a 60x objective, we acquired images 70 μm x 70 μm in size with
885 an exposure time of 250 msec and a time stamp of 500 msec to generate movies
886 30 seconds in duration. For all measured concentrations we generated n=3 movies
887 and did not observe any FoxA1 condensation. (B) FoxA1-mCherry condenses λ-
888 phage DNA molecules with Cy5 dye covalently attached to the phosphate
889 backbone of DNA (Label-IT Nucleic Acid Labeling Kit, Cy5, Mirus). (C) Unlabeled
890 FoxA1 condenses DNA (visualized with 10 nM Sytox Green). The rightmost panel
891 is a representative image of the mCherry 561 nM imaging channel, revealing that

27

892　the FoxA1 molecule does not have a mCherry fluorophore. (D) Sparse labeling of
893　FoxA1 (0.5 nM) does not influence the persistence length and contour length of λ-
894　phage DNA, as determined by hydrodynamic stretching (see Methods). (i) FoxA1
895　(purple) is sparsely bound to DNA (in grey), visualized with 10 nM Sytox Green.
896　(ii) Snapshots of unstretched DNA molecules bound at only one end to the
897　coverslip before hydrodynamic stretching in both control and 0.5 nM FoxA1
898　conditions. The yellow arrows point to the DNA molecules. (iii) Snapshots of
899　stretched DNA molecules bound at one end to the coverslip during hydrodynamic
900　stretching in both control and 0.5 nM FoxA1 conditions. (iv) Quantification of
901　stretched DNA lengths in both control (n=10) and 0.5 nM FoxA1 (n=9) conditions
902　reveals that there is no significant difference in the length under hydrodynamic
903　stretching (unpaired t-test, p=0.11). (E) FoxA1 condensates imaged in the absence
904　of DNA dye are consistent in size with that of FoxA1 condensates formed in the
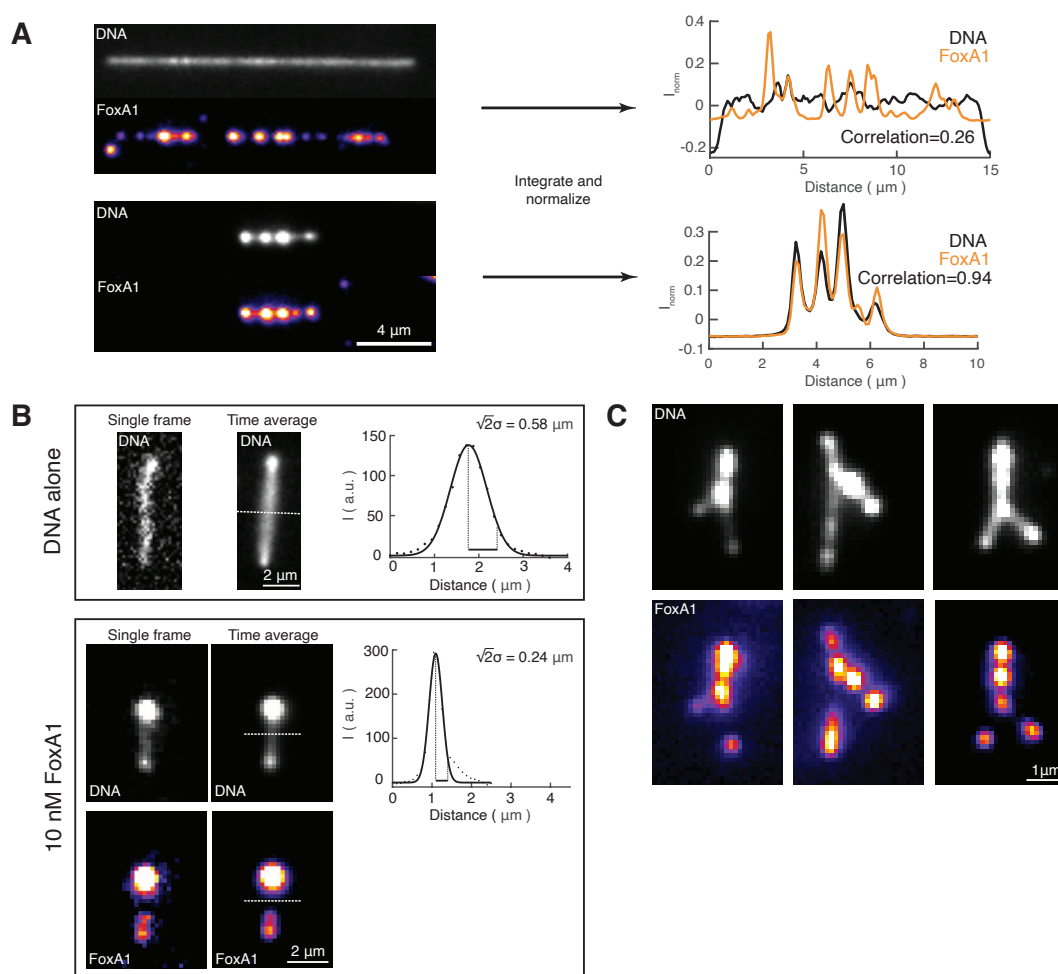905　presence of DNA dye.
906
907
908
909
910
911
912
913
914
915
916
917
918
919
920
921
922
923
924
925
926
927
928
929
930
931
932
933
934
935
936
937
938
939
940

941   **Extended Data Figure 2**

942
943   **Extended Data Figure 2: Counting FoxA1 molecules in condensates.** (A)
944   Representative image of three DNA strands with FoxA1 condensates. The inset
945   shows an area of the PEGylated glass slide void of DNA. Increased contrast reveals
946   the presence of individual spots of FoxA1 non-specifically bound to the coverslip.
947   (B) Histogram of integrated intensities of these DNA-independent FoxA1 to
948   calibrate the amount of fluorescence per molecule. The grey bars represent the
949   integrated background intensity of areas where no FoxA1 signal could be detected
950   (maximum at 289 a.u.). Pink bars represent the integrated intensity of individual
951   spots of DNA-independent FoxA1 signal. Black dotted line is a multi-Gaussian fit
952   to the pink histogram, indicating consecutive peaks in the histogram at intensities
953   of 683, 1096 and 1706 (a.u.), suggesting an integrated intensity of 400 a.u. per
954   FoxA1 molecule. Representative images (10x10 pixels) of background (left) and
955   individual DNA-independent FoxA1 spots used in this analysis are placed above
956   the histogram according to their integrated signal intensity. (C) Histogram of the
957   number of FoxA1 molecules in FoxA1 condensates on DNA, calculated based on an
958   integrated intensity of 400 a.u. per FoxA1 molecule, determined in (B). The mean
959   number of molecules is 150 per condensate. (D) Histogram of the density of FoxA1
960   molecules in the FoxA1-DNA condensates analyzed in (C). The mean value is 750
961   molecules per μm^3. These estimates represent lower bounds as previous studies
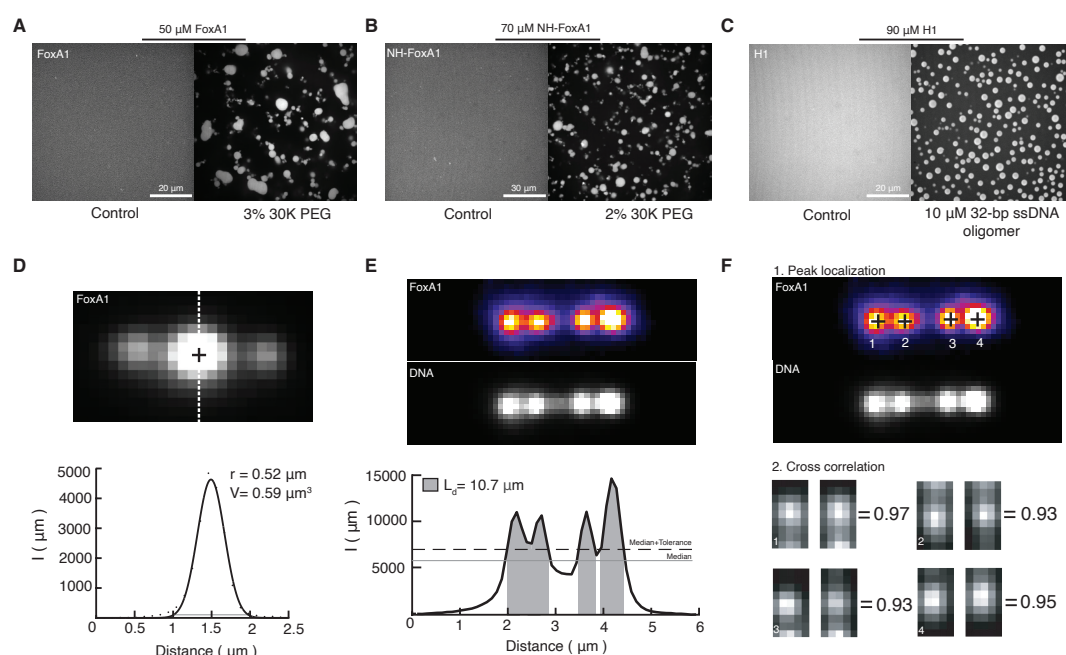
962   have demonstrated that fluorescent-based methods for estimating the number of
963   molecules neglect effects such as quenching and can underestimate the number of
964   molecules by as much as 50 fold[27].
965
966
967
968
969
970
971
972
973
974
975
976
977
978
979
980
981
982
983
984
985
986
987
988
989
990
991
992
993
994
995
996
997
998
999
1000
1001
1002
1003
1004
1005
1006
1007
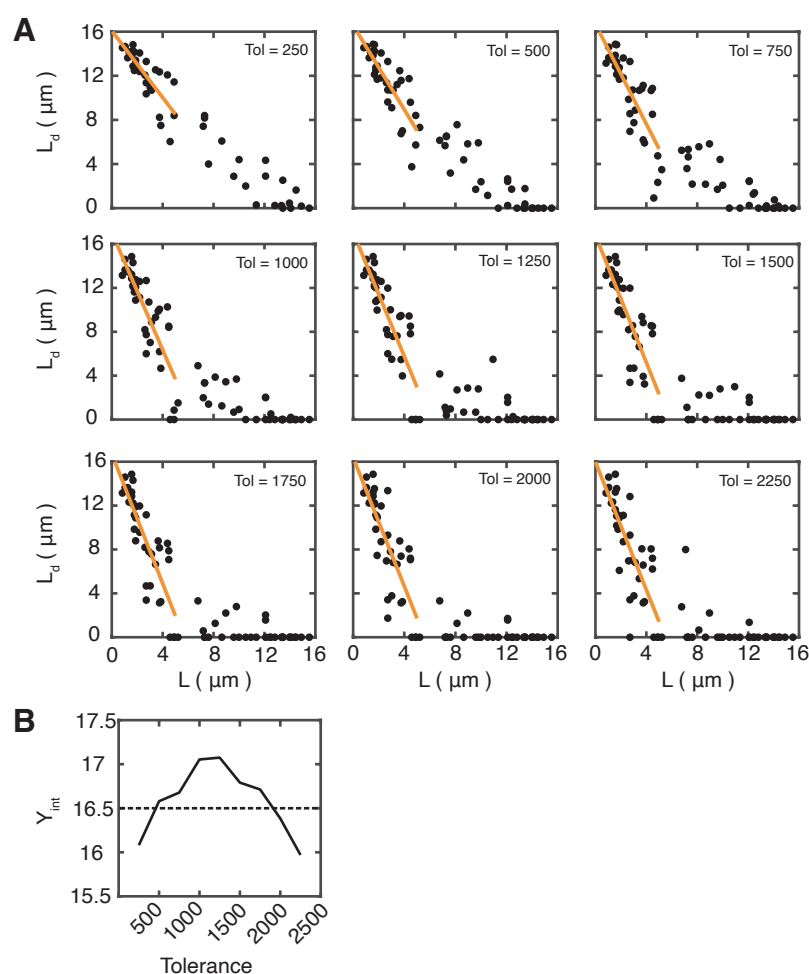1008
1009
1010

1011 **Extended Data Figure 3**

1012
1013 **Extended Data Figure 3: Quantification of FoxA1-mediated DNA**
1014 **condensation.** (A) Global cross-correlation between FoxA1 and DNA reveals
1015 FoxA1-mediatd DNA condensation. Left, representative fluorescent time-
1016 averaged projections of DNA and FoxA1 at two different end-to-end distances.
1017 Integrating both the DNA and FoxA1 signals along the axis orthogonal to the long
1018 axis of the strand gave rise to line profiles, which we normalized, and then plotted
1019 as a function of distance (DNA in black and FoxA1 in orange). We then computed
1020 the zero-lag cross-correlation coefficient defined as "Correlation" (see Methods).
1021 (B) DNA envelope width measure measures the transverse fluctuation of non-
1022 condensed DNA. Top box: DNA alone condition. Bottom box: DNA+FoxA1
1023 condition. For both conditions, we display representative fluorescent images of
1024 single frames and time-averaged projections of the DNA and FoxA1 signals. The
1025 white dashed line represents the maximum width of the DNA signal along the
1026 orthogonal axis of the non-condensed DNA. The black dots in the profile represent
1027 the background-subtracted points from the white dashed line, and the black line
1028 represents a Gaussian fit. The DNA envelope width was defined as $\sqrt{2}\sigma$, where σ
1029 is the standard deviation of the Gaussian fit. (C) Three representative examples of
1030 FoxA1-mediated zipping. These images are time-averaged projections of both
1031 FoxA1 and DNA.
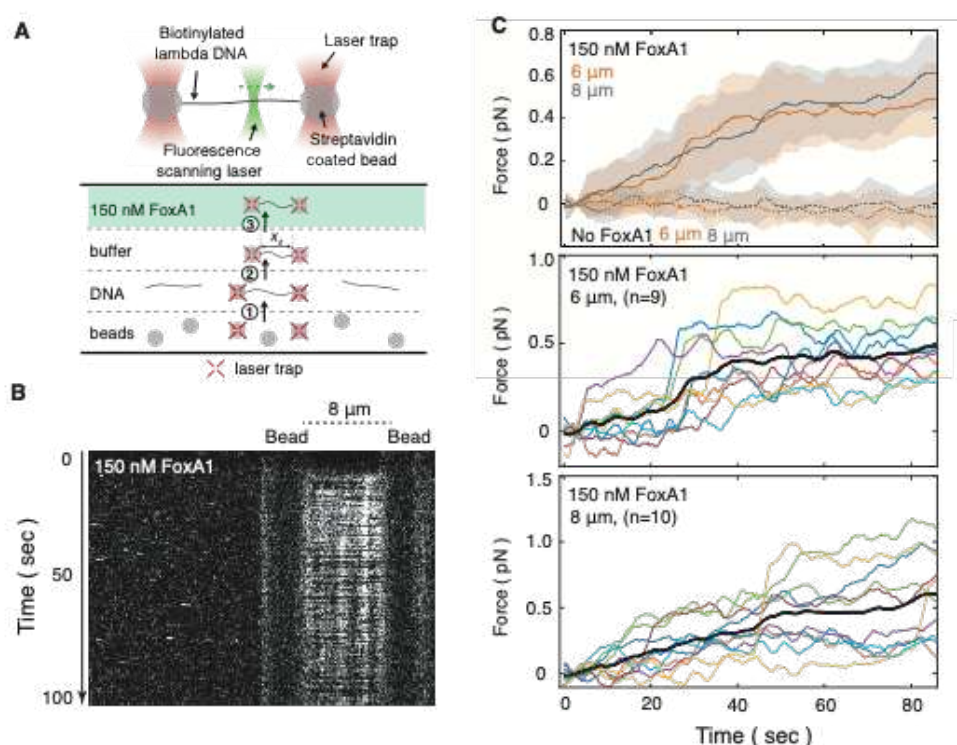1032

1033

31

1034   **Extended Data Figure 4**

1035
1036   **Extended Data Figure 4: Bulk biomolecular condensate formation and**
1037   **quantification of condensate volume, condensed DNA length, and**
1038   **condensation probability.** (A) Three per cent 30K PEG triggers FoxA1
1039   condensate formation in bulk at 50 µM in storage buffer: 20 mM HEPES (pH=6.5),
1040   100 mM KCl, 1 mM $MgCl_2$, 3 mM DTT, and 2 M Urea. (B) Two per cent 30K PEG
1041   triggers NH-FoxA1 condensate formation in bulk at 70 µM in storage buffer. (C)
1042   The addition of 10 µM 32-BP ssDNA oligomers nucleated droplets of H1 in bulk at
1043   90 µM that exhibited features of liquid-like droplets consistent with literature[28,29].
1044   These data demonstrate that H1-DNA form liquid-like condensates, which could
1045   be driven via transient cross-linking of H1 and DNA or H1-H1 interactions. Both
1046   mechanisms are accounted for in our free energy description. (D) Condensate
1047   volume quantification of a representative time-averaged projection of a FoxA1-
1048   DNA condensate, where the black cross is the condensate peak location and the
1049   white dashed line is the intersecting profile to measure the volume. Lower panel:
1050   the black dots are the profile's background-subtracted values and the solid black
1051   line is a Gaussian fit. The gray line represents the threshold value computed from
1052   the gradient of the Gaussian function that defines the edges of the condensate (see
1053   Methods). (E) Condensed DNA length quantification of a representative time-
1054   averaged projection of FoxA1 and DNA. Below: the integrated one-dimensional
1055   DNA profile is defined into condensed versus non-condensed regions using the
1056   median of the profile's median (gray) plus a tolerance (black dashed). (F) Local
1057   correlation quantification of a representative time-averaged projection of FoxA1
1058   and DNA. The condensates were localized (black crosses) and then 0.9 µm x 0.5
1059   µm boxes centered around these peaks were cropped. The correlations between
1060   the cropped regions of FoxA1 (left) and DNA (right) were then computed.
1061
1062
1063
1064
1065

32

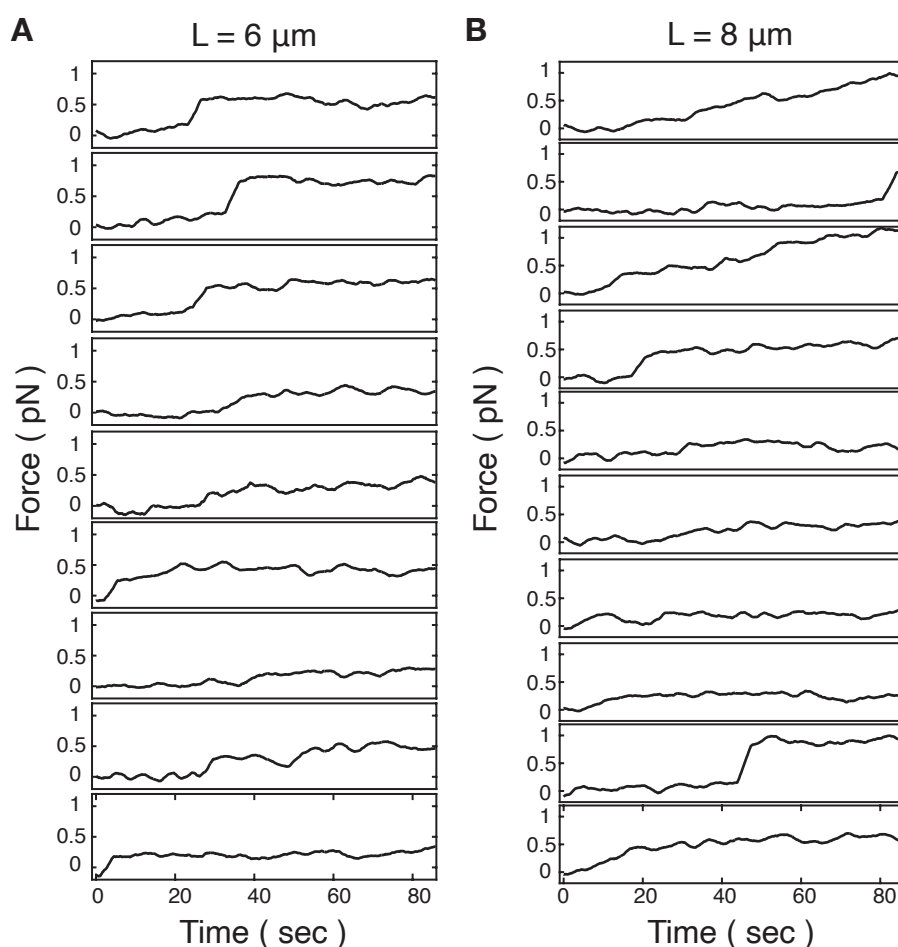1066   **Extended Data Figure 5**

1067
1068   **Extended Data Figure 5: Tolerance value calculation.** Quantification of the
1069   condensed DNA length as a function of end-to-end distance for a range of tolerance
1070   values. Condensed DNA length is computed by defining regions of condensed
1071   versus non-condensed DNA using a threshold composed of the signal's median
1072   value plus a tolerance. (A) Condensed DNA length is plotted as a function of end-
1073   to-end distance L for tolerance values from 250 to 2250 where the black dots
1074   represent the condensed DNA length for individual strands and the orange curve
1075   represent linear fits to these points for end-to-end distance below 5 μm. (B) Y
1076   intercept of the fitted linear curves. A tolerance=500 was selected as the y
1077   intercept was equal to the contour length of λ-phage DNA (16.5 μm) and gave
1078   FoxA1-DNA condensate formation up to approximately 10 μm, consistent with
1079   experimental observations (see Methods).
1080
1081
1082
1083
1084
1085
1086
1087
1088

1089   **Extended Data Figure 6**
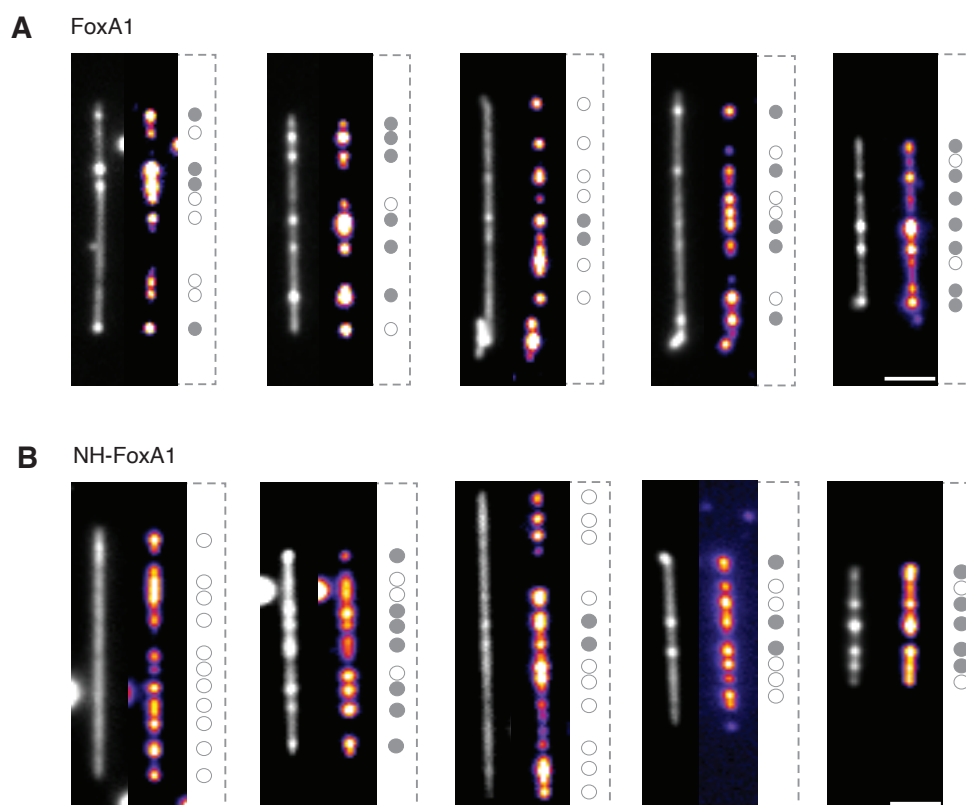

1090
1091   **Extended Data Figure 6: Optical tweezer measurements reveal that FoxA1**
1092   **generates forces on the order of 0.4-0.6 pN.** (A) Schematic outlining optical
1093   tweezer experimental design (see Methods). (B) Representative kymograph
1094   reveals that FoxA1 condensates co-localize with a single molecule of λ-phage DNA
1095   trapped between two beads at an end-to-end distance of 8 μm. (C) Force
1096   trajectories for single DNA molecules reveal forces on the order of 0.4-0.6 pN
1097   when in FoxA1-containing buffer. (Top panel) This panel displays the mean ± STD
1098   of force trajectories for each condition (n=9 for +FoxA1 with L=6 μm, n=10 for
1099   +FoxA1 with L=8 μm, n=10 for control with L=6 μm, and n=13 for control with L=8
1100   μm.). This average force is slightly higher than what we measured in Fig. 3F using
1101   fluorescence, though a comparison of the relative errors reveals that both
1102   measurements give rise to comparable forces close to their respective detection
1103   limits and within the error bars. Additionally, the optical tweezer measurements
1104   were performed at a higher FoxA1 concentration—this was due to the large
1105   amount of tubing from the entry port to the flowcell in the custom-built Lumicks
1106   system, representing a considerable amount of surface for the protein to non-
1107   specifically bind to. We found that 150 nM FoxA1 was necessary to elicit a force
1108   response and to observe FoxA1 condensate formation on DNA. We conducted
1109   these measurements in the presence of 150 nM FoxA1 in Cirillo buffer 20 mM
1110   HEPES, pH=7.8, 50 mM KCl, 3 mM DTT, 5% glycerol, 100 μg/ml BSA (solid lines)
1111   and in the presence of Cirillo buffer only (hatched lines) at end-to-end distances
1112   of L=6 (orange) or 8 μm (grey). Individual force trajectories for λ-phage DNA in
1113   the presence of buffer containing 150 nM FoxA1 with an initial end-to-end
1114   distance of 6 μm (middle panel) and 8 μm (bottom panel) reveal jumps in force,
1115   consistent with a first-order phase transition. These trajectories are re-plotted for
1116   clarity in Extended Data Fig. 7.
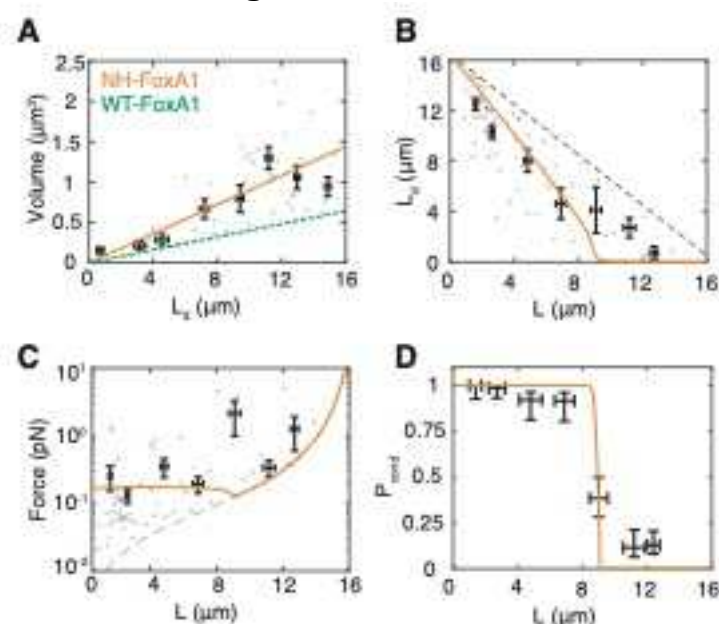
34

Extended Data Figure 7

Extended Data Figure 7: Individual temporal optical tweezer force measurements. Temporal force measurements from optical tweezers with an initial end-to-end distance of 6 μm (n=9 strands) (A) and 8 μm (n=10 strands) (B) in the presence of 150 nM FoxA1. These data are the same as in Extended Data Fig. 6c, and are re-plotted individually for clarity.
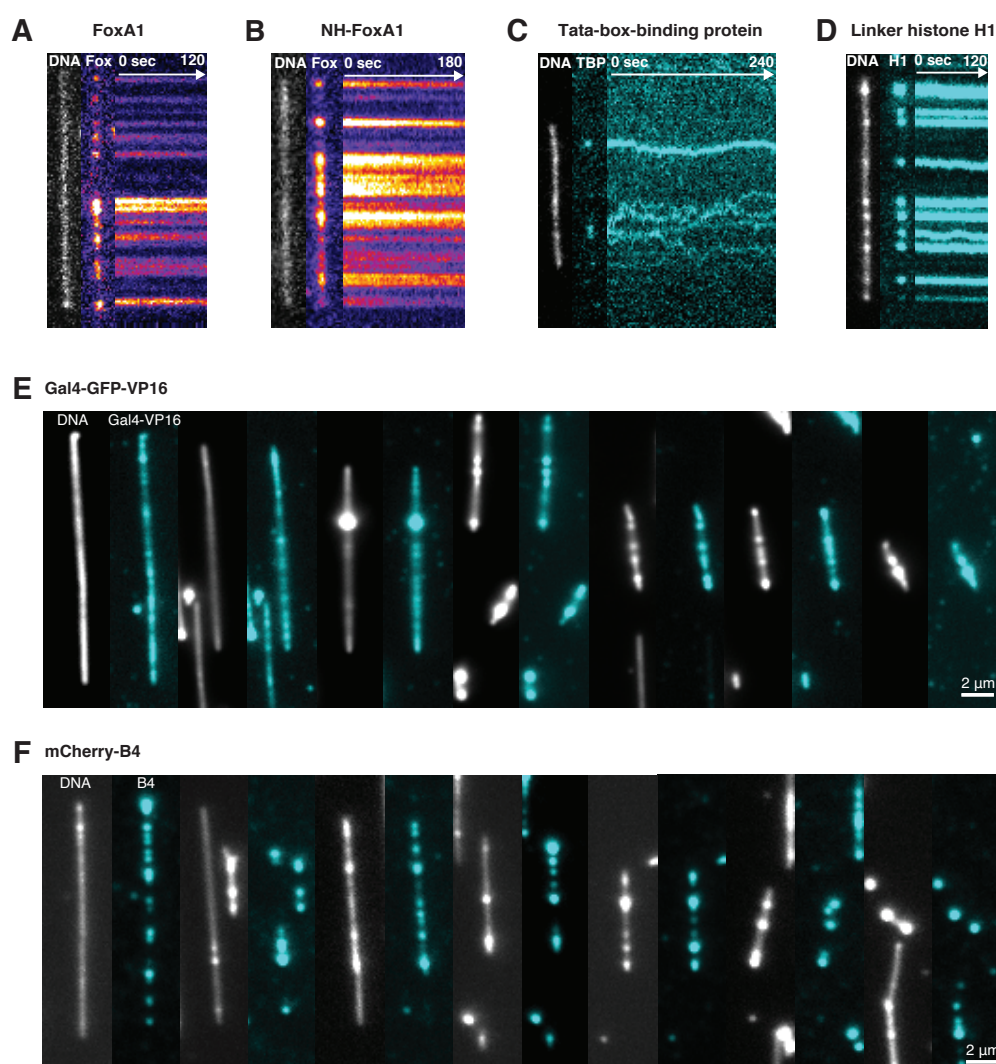
1141 **Extended Data Figure 8**

1142
1143 **Extended Data Figure 8: Bistability of FoxA1-mediated DNA condensation.**
1144 (A) Representative time-averaged projections of DNA and FoxA1 signals show
1145 that FoxA1 condenses DNA in an all-or-nothing manner. On the right side of each
1146 pair of images, we localized the FoxA1 condensates and showed whether FoxA1
1147 condenses DNA (filled-in gray circle) or not (open circle). Interestingly, there is a
1148 mixed population, revealing the bistable nature of the condensation process. (B)
1149 Representative images of condensation bistability for the sequence-specific DNA-
1150 binding mutant, NH-FoxA1. Scale bars = 2 μm.
1151
1152
1153
1154
1155
1156
1157
1158
1159
1160
1161
1162
1163
1164
1165
1166
1167
1168

1169 **Extended Data Figure 9**

1170
1171 **Extended Data Figure 9: Quantification of NH-FoxA1-mediated DNA**
1172 **condensation.** (A) Condensate volume as a function of condensed DNA length
1173 (L_d). The grey dots represent individual strands (n=47) and the data is binned
1174 every 2 μm (mean ± SEM). The individual data are points are fit with a linear curve
1175 with a slope of 0.09 μm² given in orange. The green dashed line is the WT-FoxA1
1176 fit (slope=0.04 μm²). (B) Condensed DNA length as a function of end-to-end
1177 distance. The black dots represent individual strands (n=70) and the data is
1178 binned every 2 μm (mean ± SEM). The orange curve is the expression computed
1179 from the theoretical description with parameter values determined through error
1180 minimization (see Methods). The black hatched line represents the DNA's contour
1181 length (16.5 μm) minus the end-to-end distance. (C) The force that the condensate
1182 exerts on the non-condensed DNA as a function of end-to-end distance. The grey
1183 dots represent individual strands (n=68) and the data is binned every 2 μm (mean
1184 ± SEM). The orange curve is the expression computed from the theoretical
1185 expression of L_d versus L from panel B for the force. NH-FoxA1 generates forces at
1186 roughly 0.17 pN. The dashed black line represents the force exerted on the non-
1187 condensed strand when L_d=0. (D) Probability for NH-FoxA1 to form a DNA-FoxA1
1188 condensate reveals a sharp transition at a critical end-to-end distance. Local
1189 correlations of individual FoxA1 condensates with DNA (Extended Data Fig. 4c)
1190 are calculated, binned into 2-μm-width bins, and P_{cond} is calculated (see Methods).
1191 There are a total number of n=361 condensates used for this analysis. The dashed
1192 lines represent the P_{cond} value as computed within the bin with ± SD for the
1193 strand's end-to-end distance. The confidence intervals for P_{cond} are computed by
1194 computing the 95% confidence interval of a beta-distribution (see Methods). The
1195 orange curve represents P_{cond} computed from the theoretical description with
1196 parameter values determined through error minimization.
1197
1198
1199
1200
1201

1202   **Extended Data Figure 10**

1203
1204   **Extended Data Figure 10: Dynamics of DNA-binding proteins.** (A)
1205   Representative images of FoxA1 condensates on DNA. The kymograph reveals
1206   FoxA1 condensates do not move on DNA. (B) NH-FoxA1 condensates remain
1207   stable on DNA and do not move. (C) TBP condensates exhibit diffusive-like
1208   behavior on DNA. (D) Similar to FoxA1 condensation, H1 condensates do not
1209   exhibit diffusive-like behavior on DNA. (E) Representative images of Gal4-GFP-
1210   VP16-mediated DNA condensation. DNA was imaged with 10 nM Sytox Orange.
1211   (F) Representative images of mCherry-B4-mediated DNA condensation. DNA was
1212   imaged with 10 nM Sytox Green.

Supplementary Information

1   Thermodynamic description of DNA-protein condensation

We consider the free energy associated with nucleating a condensate that contains DNA and FoxA1. The free energy of this process contains volume and surface contributions of the DNA-protein condensate as well as the free energy of the DNA polymer outside the condensate,

$$F(L, L_d) = F_d(L_d) + F_p(L, L_d), \tag{1}$$

where L is the end-to-end distance of the DNA, L_d is the length of condensed DNA, F_d is the free energy of the condensate, and F_p is the free energy of the DNA polymer outside the condensate. Assuming that the DNA co-condenses with the protein to form a dense condensed phase with defined volume fraction of DNA, the droplet volume and the length of condensed DNA are linearly related, $V = \alpha L_d$, or $R^3 = \frac{3\alpha}{4\pi} L_d$, where $1/\alpha$ describes the DNA packing density given as DNA length per condensate volume. We can then obtain the condensate free energy of nucleating a condensate as a function of L_d and end-to-end distance L as

$$F_d(L_d) = -\nu\alpha L_d + \gamma 4\pi \left(\frac{3\alpha}{4\pi}\right)^{2/3} L_d^{2/3}, \tag{2}$$

where ν is the condensation free energy per volume, and γ is the surface tension of the condensate. The free energy of the polymer $F_p(L, L_d)$ is related to the external force applied to pin the free DNA polymer and its associated chemical potential by

$$f_{\text{text}} = \left. \frac{\partial F_p}{\partial L} \right|_{L_d}, \quad \mu_p = -a \left. \frac{\partial F_p}{\partial L_d} \right|_L, \tag{3}$$

where a is the length of a base pair. The force-extension relation for λ-phage DNA has been extensively studied previously, and here we use the phenomenological force-extension curve of the worm-like-chain model for λ-phage DNA (14) with contour length, L_c (for λ-phage DNA L_c = 16.5 μm). If a length L_d of the DNA is condensed, the extension of the non-condensed strand is $x = \frac{L}{L_c - L_d}$. The force on the strand then can be expressed as

$$f_{\text{text}} = \frac{k_B T}{P} \left(\frac{1}{4} \frac{1}{(1-x)^2} - \frac{1}{4} + x \right), \tag{4}$$

where k_B is the Boltzmann constant, T is the temperature, and P is the persistence length of DNA. For what follows we define $\kappa = \frac{k_B T}{P}$. From this expression of the force and its relation to the free energy of the DNA polymer (equation 3), we can obtain the free energy of the DNA polymer outside the condensate as $F_p(L, L_d) = \int_0^L dL' f_{\text{text}}(L', L_d)$, leading to

$$F_p(L, L_d) = \kappa \left(\frac{1}{4} \frac{(L_c - L_d)^2}{L_c - L_d - L} - \frac{1}{4} L + \frac{1}{2} \frac{L^2}{L_c - L_d} - \frac{1}{4}(L_c - L_d) \right) \tag{5}$$

The total free energy associated with nucleating a FoxA1-DNA condensate on a DNA strand reads:

$$F(L, L_d) = -\nu \alpha L_d + \gamma 4\pi \left(\frac{3\alpha}{4\pi} \right)^{2/3} L_d^{2/3} + \kappa \left(\frac{1}{4} \frac{(L_c - L_d)^2}{L_c - L_d - L} - \frac{1}{4} L + \frac{1}{2} \frac{L^2}{L_c - L_d} - \frac{1}{4}(L_c - L_d) \right) \tag{6}$$

2

The equilibrium between condensate and polymer is given by $\frac{\partial F}{\partial L_d} = 0$, which is equivalent to equilibrating the chemical potentials of the condensate and free polymer,

$$a\frac{\partial F}{\partial L_d} = \mu_d(L_d) - \mu_p(L, L_d) = 0, \tag{7}$$

with

$$\mu_p(L, L_d) = -a\kappa\left(\frac{1}{4} + \frac{L^2}{2(Lc - Ld)^2} + \frac{(Lc - Ld)^2}{4(Lc - L - Ld)^2} - \frac{Lc - Ld}{2(Lc - L - Ld)}\right) \tag{8}$$
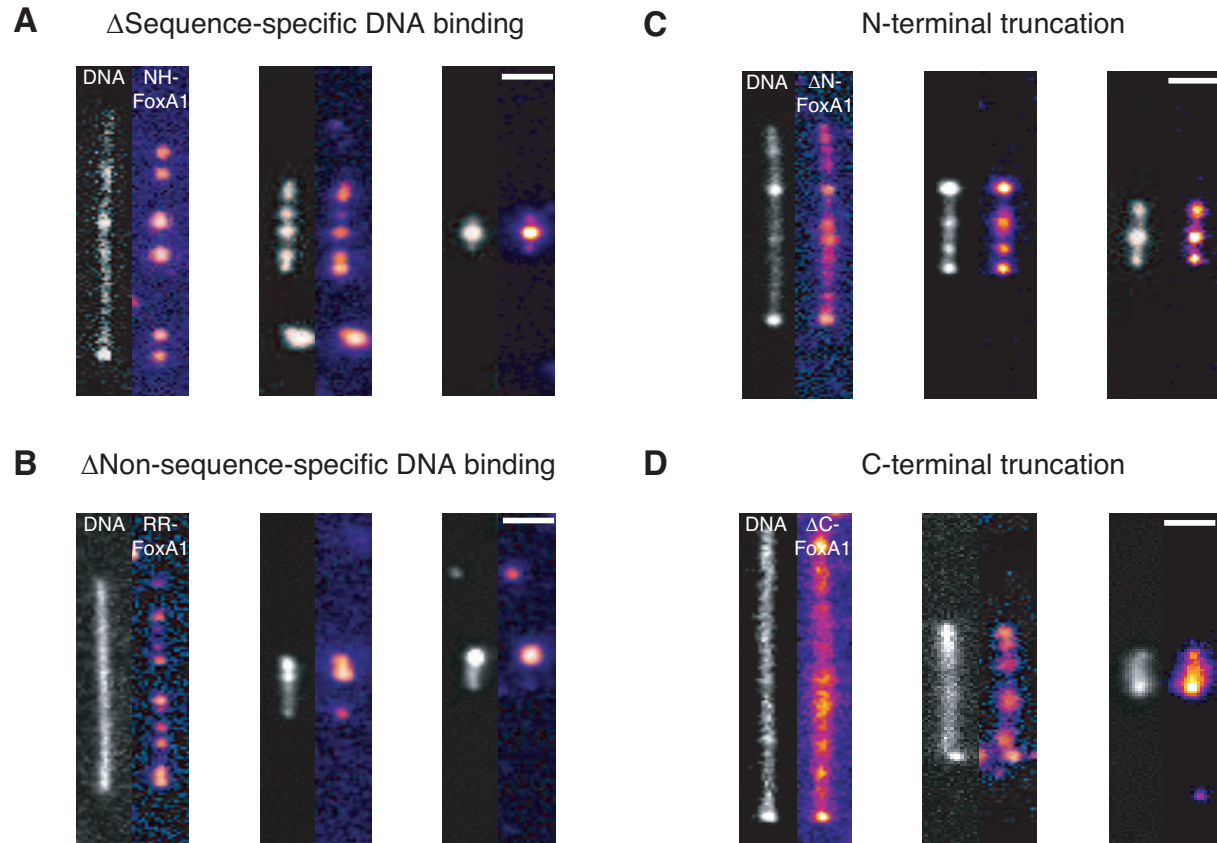
Using the expression for the total free energy, we can vary the length L_d of condensed polymer and obtain profiles for the free energy as a function of L_d, which depend on the end-to-end distance L (see Fig. 3b). For L values close to 0—where the strand is not under tension—we observe that there is a minimum of F for L_d close to L_c. This means that, at this end-to-end distance, FoxA1 has mediated the generation of a FoxA1-DNA condensate using almost all of the DNA in the strand. As L increases, however, the local minimum shifts to lower values of L_d and ultimately F at the minimum becomes higher than the free energy without condensate $F(L_d = 0)$, giving rise to a branch of metastable states. For even higher L values, the metastable state disappears and the global minimum is at $L_d = 0$ (Fig. 3b). This sharp transition corresponds to a first-order phase transition. Simple scaling arguments are useful to generate intuition for the conditions necessary for condensate formation, and for the condensate to pull DNA. Briefly, there are three energy scales associated with this problem: the energy associated to create a droplet, which is $\nu\alpha L$; the surface energy of scale $4\gamma\pi\left(\frac{3\alpha}{4\pi}\right)^{2/3}L^{2/3}$; and lastly the energy scale associated to the non-condensed polymer $L\frac{k_BT}{P}$. First, to create a droplet, $\frac{\nu(4\pi)^{2/3}(\alpha L)^{1/3}}{4\pi3^{2/3}\gamma} > 1$. Once condensation is favorable, in order for the droplet to pull DNA, $\frac{\nu\alpha P}{k_BT} > 1$. Notably, fitting the parameter values (see Methods) demonstrated that, at low L, the free energy gained by the system is on order of 1-2 k_BT, implying that stochasticity

3

is relevant for the condensation process. To account for the inherent stochastic nature of the condensation, we compute the probability of nucleating a DNA-protein condensate of size L_d using Boltzmann distributions from the corresponding energy profiles,

$$P(L_d) = \frac{e^{-\beta F(L,L_d)}}{\int_0^{L_c-L} dL'_d e^{-\beta F(L,L'_d)}} \tag{9}$$

where $\beta = \frac{1}{k_B T}$. To determine the relationship between L_d and L, we compute the mean L_d value of these Boltzmann distributions: $\bar{L}_d = \int_0^{L_c-L} L_d P(L_d) dL_d$ which then allows us also to calculate the magnitude of the condensation forces using the worm-like chain model given in Eq. (4).

2 Supplementary Information Figures

A   ΔSequence-specific DNA binding

B   ΔNon-sequence-specific DNA binding

C   N-terminal truncation

D   C-terminal truncation

Figure 1: Representative images of sequence-specific-binding NH-FoxA1 mutant (A) non-sequence-specific-binding RR-FoxA1 mutant (B) N-terminal FoxA1 truncation (C) and C-terminal FoxA1 truncation (D). The scale bars are 2 μm. DNA is imaged with 10 nM Sytox Green. Note that the contour length of each DNA molecules is constant (16.5 μm) but the end-to-end distance is different.
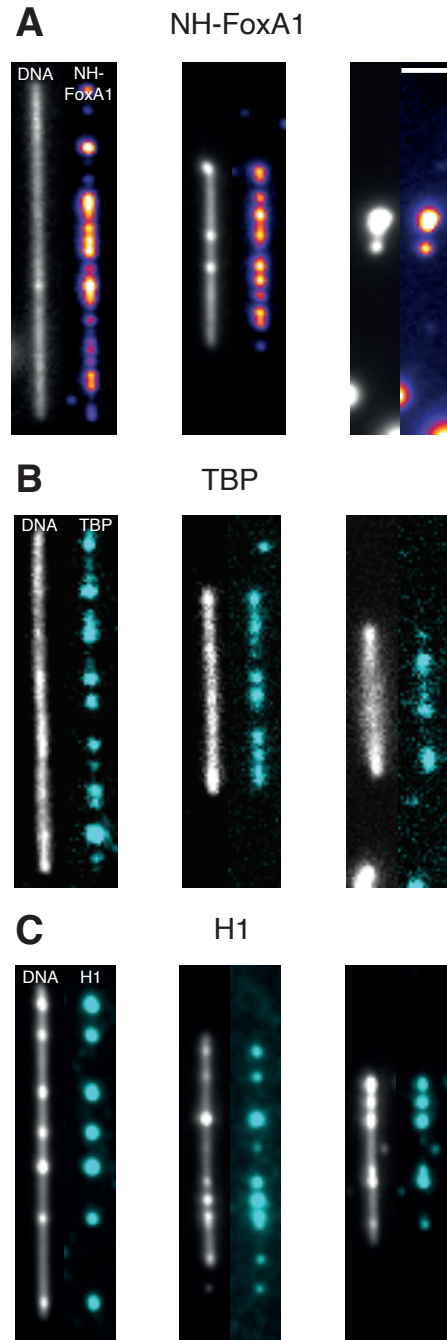
Figure 2: Representative images for NH-FoxA1 (A) Tata-box-binding protein (B) and somatic linker histone H1 (C). The images are time-averaged projections of movies for NH-FoxA1 and H1 but single images for TBP owing to TBP's diffusivity. The scale bar is 2 μm.